

**ESTIMATING THE COMPOSITION OF MULTICOMPONENT PARTICLE  
SLURRIES USING FOCUSED BEAM REFLECTANCE MEASUREMENT**

A Dissertation  
Presented to  
The Academic Faculty

by

Tristan James Kernick

In Partial Fulfillment  
of the Requirements for the Degree  
Master of Science in the  
School of Chemical and Biomolecular Engineering

Georgia Institute of Technology  
May 2018

**COPYRIGHT © 2018 BY TRISTAN JAMES KERNICK**

**ESTIMATING THE COMPOSITION OF MULTICOMPONENT PARTICLE  
SLURRIES USING FOCUSED BEAM REFLECTANCE MEASUREMENT**

Approved by:

Dr. Martha A. Grover, Advisor  
School of Chemical and Biomolecular  
Engineering  
*Georgia Institute of Technology*

Dr. Athanasios Nenes  
School of Chemical and Biomolecular  
Engineering  
*Georgia Institute of Technology*

Dr. Yoshiaki Kawajiri, Advisor  
School of Chemical and Biomolecular  
Engineering  
*Georgia Institute of Technology*

Dr. Ronald W. Rousseau, Advisor  
School of Chemical and Biomolecular  
Engineering  
*Georgia Institute of Technology*

Date Approved: December 5, 2017

## ACKNOWLEDGEMENTS

I would like to acknowledge the Consortium for Risk Evaluation with Stakeholder Participation for their generous funding of this research project, and for their continual feedback throughout the research process. I thank Chris Guenther, who organized the shipping of our simulant sample free of charge. I would like to thank present and past members of the Grover, Kawajiri, and Rousseau groups for their friendship and suggestions throughout my time at Georgia Tech. Special thanks go to Dan Griffin, Luis Encarnacion-Gomez, Matt McDonald, Nils Persson, Youngjo Kim, Mike McBride, Krysten Minnici, and Bailey Risteen for sharing lab and office space with me and providing daily input to help me complete this thesis.

I give my sincere thanks to my advisors Dr. Martha Grover, Dr. Yoshiaki Kawajiri, and Dr. Ronald Rousseau for guiding me in my research. Without your suggestions and ability to give me a push in the right direction, I would not have been able to complete this thesis. I extend my thanks to Jacqueline Mohalley-Snedeker, who provided invaluable support during the writing process, and without whom I would not have gotten moving toward this goal.

I would like to thank my friends Kong Wong, Nathan Ellebracht, Jason Lee, and Michael Dunn for their moral support along my academic journey. I thank Mathilda Avirett-Mackenzie for providing me with the additional help and motivation required to get this thesis finished.

Finally and most importantly, I would like to thank my family whose love, support, and belief in me has made this thesis possible. I dedicate this thesis to you.

## TABLE OF CONTENTS

ACKNOWLEDGEMENTS .....	iii
LIST OF TABLES .....	vi
LIST OF FIGURES .....	vii
LIST OF SYMBOLS AND ABBREVIATIONS .....	xi
SUMMARY .....	xii
CHAPTER 1 INTRODUCTION .....	1
CHAPTER 2 BACKGROUND AND THEORY .....	5
2.1 FBRM Operating Principles .....	5
2.2 Qualitative Uses of FBRM.....	6
2.2.1 Qualitative Monitoring and Crystallization Control.....	6
2.2.2 Monitoring Polymorphic Transitions.....	8
2.3 Quantitatively Relating CLH to PSD.....	10
2.3.1 Linear Model.....	10
2.3.2 First-principles Approaches .....	13
2.3.2.1 Geometric Modeling .....	13
2.3.2.2 Modeling Backscattering .....	16
2.3.3 Empirical Approaches.....	17
2.4 Regressing PSD from CLH.....	20
CHAPTER 3 METHODS .....	22
3.1 Equipment Setup.....	22
3.2 Solid-phase Monitoring .....	23
3.3 Six-component Waste Simulant.....	23
3.4 Experimental Methods .....	26
3.5 Computational Methods.....	27
CHAPTER 4 RESULTS & DISCUSSION .....	30
4.1 Component Fingerprints .....	30
4.2 Chord Length Error Analysis.....	48

4.3	Model Accuracy.....	51
4.4	Model Modifications.....	63
CHAPTER 5 CONCLUSIONS & RECOMMENDATIONS.....		69
REFERENCES .....		74

## LIST OF TABLES

Table 1 – Department of Energy (DOE) waste simulant. Solids are mixed with deionized water to achieve a total solids content of 12 wt%. Multiplying this solid fraction by the percentages in the third row yields the final amounts in the fourth row .....	24
Table 2 – Slopes of the linear regressions shown in Figure 8. The slope for silicon carbide is reported twice: first for the regression including all data, and second for the regression through only the region where its mass and counts appear to vary linearly (between 0 and 0.2 g). Each slope is presented with its corresponding 95% confidence interval .....	37
Table 3 – Slopes of the linear regressions for various additivity experiments, compared to their chord count slopes in single-component mixtures. Like in Table 2, 95% confidence intervals are tabulated as well.....	46
Table 4 – Standard deviation of total counts measurement, as a percent of the total counts. Deviations were calculated for chord counts both below and above 30 $\mu\text{m}$ .....	49
Table 5 – $R^2$ coefficients for the linear regression between chord counts and solid mass. These coefficients were calculated for counts above and below 30 $\mu\text{m}$ ; SiC considered only the linear region at small mass fractions shown in Figure 7.....	50

## LIST OF FIGURES

Figure 1 – Schematic of FBRM probe operation. (A) The probe emits a laser that rotates at a fixed speed. (B) As the laser beam crosses particles, the probe detects the backscattered light. The duration of each pulse of backscattered light is translated into a chord length by multiplying by the laser rotation speed .....	5
Figure 2 – FBRM visualization of imidacloprid polymorphic transition from Form II (needle-like) to Form I (flaky). (A) Unweighted (left curves) and square-weighted (right curves) CLHs, plotted at different times during the crystallization experiment. (B) Groupings of fine counts (0-50 $\mu\text{m}$ ), medium counts (50-150 $\mu\text{m}$ ), and coarse counts (150-300 $\mu\text{m}$ ) at every time point during the crystallization experiment. Reproduced with permission from Zhao <i>et al</i> .....	9
Figure 3 – Counts versus solid fraction for different size ranges of calcite particles, reproduced with permission from Heath <i>et al</i> .....	12
Figure 4 – Illustration of chord splitting on a photomicrograph of a 50 $\mu\text{m}$ glass bead. The red line through the image represents the theoretical travel path of an FBRM laser. Dashed lines are drawn to show where the laser intersects with the dark parts of the particle.....	15
Figure 5 – OptiMax™ system with attached probes .....	22
Figure 6 – Micrographs of the six simulant components. (A) Silicon carbide, (B) tungsten alloy, (C) 45-90 $\mu\text{m}$ soda-lime glass beads, (D) alumina ( $\text{Al}_2\text{O}_3$ ), (E) sand ( $\text{SiO}_2$ ), (F) 841-1190 $\mu\text{m}$ soda-lime glass beads .....	25
Figure 7 – FBRM histograms for all six simulant components. The weight fractions of the three smallest components used to create these fingerprints are given in Table 1. The large components used 15 g of solid material in 500 mL of deionized water to produce more chord counts. (A) All components plotted on an axis automatically sized for SiC, showing the disparity in total counts between SiC and the other components. (B) Component fingerprints, zoomed in to show the shapes of tungsten and small glass spheres. (C) Component fingerprints, zoomed in to show the shapes of the three largest components. (D) Component histograms plotted on a logarithmic y-axis.....	30
Figure 8 – Figure 8 – Square-weighted chord length histograms for all components. Histograms were recorded with the same material amounts as Figure 7. Note that the y-axis is not listed in units of $\mu\text{m}^2$ , as would be expected for length-square weighting. Mettler-Toledo’s software rescales the y-axis so that the numbers are smaller and more representative of the expected counts of large particles. (A) All histograms plotted on axes that are automatically scaled for SiC. (B) The y-axis is reduced to show the shapes of the $\text{Al}_2\text{O}_3$ , $\text{SiO}_2$ , and large glass bead histograms .....	32
Figure 9 – Fingerprints of the six simulant components. (A) Plots of all six fingerprints, with y-axis scaled to fit the entire SiC histogram. (B) Same curves as Figure 9A, but with the y-axis adjusted to show the scale of the three largest components.....	33
Figure 10 – Chord length histograms of all six components, normalized by the number of particles used to record each data set .....	34

Figure 11 – Results from linearity tests of each simulant component. The blue points are experimental data, and the dotted red line represents a linear regression to the data. All components but silicon carbide are roughly linear. Linearity is assessed in terms of solid mass. The error bars represent the standard deviation of the chord counts across the 10 minutes of averaging. They were calculated using repeated observations of the same system at intervals of 15 s, making them representative of the measurement noise .....38

Figure 12 – Chord length histograms from the experiments shown in Figure 9. A fixed mass of each simulant component is added to 500 mL of water at regular time intervals. Each histogram shown in this figure has been averaged over five minutes .....40

Figure 13 – Total counts for each simulant component, plotted against slurry density to examine linearity. The blue points are experimental data, and the dotted red line represents a linear regression to the data. The error bars represent the standard deviation of the chord counts across the time interval of averaging .....40

Figure 14 – Silicon carbide total counts at small solid fractions. The blue points are experimental data, and the dashed line is a linear regression through the first three points, to show that a linear chord count region does exist. The total counts at 1 g are on the same order of magnitude as the counts at 10 g in Figure 11. The error bars are the same as those in Figure 11, where they represent the chord count standard deviations across the averaging intervals .....41

Figure 15 – Linear combinations of the six component fingerprints, plotted alongside FBRM data taken from the component combinations mixed in 500 mL water. (A) 0.7 g of SiO<sub>2</sub> and 1 g of large glass beads. (B) 2.4 g of Al<sub>2</sub>O<sub>3</sub> and the two components from 15A. (C) 25.6 g of small glass beads added to the components from 15B. (D) 2.7 g of Tungsten shavings and the four components from 15C. (E) 0.1 g of SiC added to the components from 15D, completing the simulant. (F) Zoom of Figure 15B to show histogram above 30 μm.....43

Figure 16 – Additivity results for small glass spheres and tungsten shavings. (A) Total counts versus mass, for glass in the presence of 3.3 g tungsten (blue curve) and in pure water (red curve). (B) Total counts versus mass, for tungsten in the presence of 27 g glass (blue curve) and in pure water (red curve). The error bars represent the chord count standard deviations across the averaging intervals.....45

Figure 17 – Chord length histograms recorded for samples of 27 g of small glass beads in 500 mL water, measured on two different days. Blue curve is from the measurement used for Figure 16A, red curve is from the measurement used for Figure 16B.....47

Figure 18 – Additivity results for SiC and tungsten shavings. (A) Total counts versus mass, for tungsten in the presence of 0.1 g SiC (blue curve) and in isolation (red curve). (B) Total counts versus mass, for SiC in the presence of 3.3 g tungsten (blue curve) and in isolation (red curve) – the linear regressions are made using only data between 0 and 0.2 g of SiC .....48

Figure 19 – Composition estimates from the model for a mixture of 3.3 g tungsten and 27 g of small glass beads. (A) Composition estimate made by the unmodified linear model. The blue bars indicate the slurry’s true composition, and the yellow bars indicate the model’s estimate. (B) Plot

of the actual measured CLH, the best-fit CLH using the linear model, and the linear model's prediction of what the ideal CLH should look like. (C) Composition estimate using the AIC component selection step. (D) CLH plot for 19C. (E) Composition estimate using the AIC component selection step and excluding counts below 30  $\mu\text{m}$ . (F) CLH plot for 19E.....53

Figure 20 – Real-time composition estimate for the experiment performed in Figure 16A and Figure 19. The solid lines indicate the model-predicted composition, and the dashed lines represent the actual composition. The AIC component-selection step is used in this model, and the model considers all chord counts between 1 and 1000  $\mu\text{m}$  .....55

Figure 21 - Real-time composition estimate for the experiment performed in Figure 16B. The solid lines indicate the model-predicted composition, and the dashed lines represent the actual composition. The AIC component-selection step is used in this model, and the model considers all chord counts between 1 and 1000  $\mu\text{m}$  .....56

Figure 22 – Composition estimates for a mixture of 0.1 g SiC and 3.3 g tungsten shavings. (A) Composition estimate using the AIC component selection step. (B) Same data as Figure 17A, but with the y-axis zoomed to show mass estimates other than large glass beads. (C) Composition estimate using the AIC component selection step, excluding counts shorter than 30  $\mu\text{m}$ . (D) Same data as Figure 22C, with the y-axis zoomed to show mass estimates other than large glass beads. (E) CLH plot for Figure 22A. (F) CLH plot for Figure 22C .....57

Figure 23 – Composition estimates for slurry containing 2.4 g alumina, 0.7 g silica, and 1 g of large glass beads. (A) Model estimate compared to actual composition, using the full range of chord lengths. (B) CLH plot showing the FBRM data for the mixture, the model's best-fit CLH, and the model's prediction of what the CLH should be. (C) Model estimate of composition, using only counts longer than 30  $\mu\text{m}$ . (D) Same curves as Figure 23B, but using counts longer than 30  $\mu\text{m}$  .....59

Figure 24 – Composition estimate for the full simulant containing 0.1 g SiC, 2.7 g tungsten, 26 g small glass beads, 2.4 g alumina, 0.7 g silica, and 1 g large glass beads. Silicon carbide is present in this small concentration so that its chord counts remain linear. The model operated on the full range of chord length bins, from 1 to 1000  $\mu\text{m}$ . (A) Model estimate compared to actual composition. (B) Zoom of (A) to show that SiC is correctly estimated, and all three large components are absent. (C) CLH plot showing the model prediction and fit.....61

Figure 25 – Composition estimate for the full simulant containing 0.1 g SiC, 2.7 g tungsten, 26 g small glass beads, 2.4 g alumina, 0.7 g silica, and 1 g large glass beads. The model operated only on chord length bins between 30 and 1000  $\mu\text{m}$  to produce this estimate. (A) Model estimate compared to actual composition. Alumina, silica, and both glass bead sizes show zero mass. (B) CLH plot using the whole simulant and excluding counts below 30  $\mu\text{m}$  .....62

Figure 26 – (A) Composition estimates for a mixture of 0.1 g SiC and 3.3 g tungsten, with square-weighted data in the model. Including the extra data set removes all of the excess amounts predicted in the unweighted-only model. This model incorporates the AIC and excludes counts

smaller than 30  $\mu\text{m}$ . (B) CLH plot of SiC-tungsten mixture. (C) CLH plot of SiC-tungsten mixture, using square-weighted data.....64

Figure 27 – (A) Composition estimates for a mixture of 27 g small glass beads and 3.3 g tungsten, with square-weighted data in the model. (B) CLH plot of glass-tungsten mixture. (C) CLH plot using square-weighted data.....66

Figure 28 – (A) Composition estimates for the completed simulant containing 0.1 g SiC, 2.7 g tungsten, 26 g small glass beads, 2.4 g alumina, 0.7 g silica, and 1 g large glass beads, with square-weighted data in the model. (B) CLH plot of this mixture. (C) CLH plot using square-weighted data.....67

## LIST OF SYMBOLS AND ABBREVIATIONS

- $\alpha$  — angle between laser path and particle
- $a$  — ellipse major axis
- $b$  — ellipse minor axis
- AIC* — Aikake information criterion
- $c$  — vector containing chord length histogram
- CLH* — chord length histogram
- $d$  — shortest distance between center of particle and measured chord
- DOE* — Department of Energy
- $F$  — number of chord length fingerprints
- FBRM* — focused beam reflectance measurement
- $l$  — chord length
- $\hat{L}$  — normalized likelihood function
- $m$  — number of bins in chord length histogram
- MSE* — mean squared error
- $n$  — number of bins in particle size distribution
- NETL* — National Energy Technology Laboratory
- $p$  — probability of recording a chord of length  $l$
- PSD* — particle size distribution
- $s$  — particle size (often, equivalent spherical diameter)
- $r$  — ellipse aspect ratio,  $a/b$
- $u$  — column of transformation matrix  $U$ , has length  $m$
- $U$  — transformation matrix for computing CLH for a given PSD
- $\tilde{U}$  — matrix  $U$ , multiplied by  $V$
- $V$  — total volume of liquid in the observed slurry
- $x$  — vector containing particle size distribution

## SUMMARY

This thesis uses focused beam reflectance measurement (FBRM) in conjunction with a linear empirical model to measure the solid concentration in a nuclear waste simulant *in situ*. Nuclear waste represents a significant environmental hazard at the Hanford site in Washington State, and the research in this thesis works towards developing a means of monitoring the solid particles present in nuclear waste. The waste simulant, which consisted of six individual components mixed with water, was placed in a stirred vessel and monitored with FBRM at a range of concentrations. The assumptions inherent to the linear model, which incorporates experimentally obtained FBRM histograms from each of the simulant components, were assessed, and the model was applied to two- and three-component mixtures before being used to estimate the composition of the complete simulant. The linear model was capable of estimating the composition of the two-component system containing glass beads and tungsten shavings, and it was able to track changes in composition over time for this simplified system. For the other four components, the model yielded less accurate results. All three large components (alumina, silica, and glass beads from a larger size range) produced much fewer FBRM counts per unit mass of simulant than the smallest three components, making them difficult to detect when the small components were included in the monitored mixture. Silicon carbide, the smallest component in the waste simulant, saturated the FBRM probe at the concentration specified in the simulant, thereby impeding detection of the other five components. Ultimately, the model presented in this thesis can produce accurate composition estimates if the materials being used behave linearly under FBRM observation. For a simple two-component system with particles that backscatter a large percentage of incident light, the linear model has yielded accurate composition estimates with computation times on the order of a few seconds. Materials that generate few chord counts or

materials with nonlinear chord count behavior require more advanced models and signal processing to predict composition from their chord length histograms. For the full six-component simulant, the model used in this thesis lacked sufficient complexity to describe the behavior of the system. Further work is necessary to enhance the model's ability to interpret data produced by multicomponent mixtures.

# Chapter 1. Introduction

## 1.1 Global Motivation

The Hanford site in Washington State held 53 million US gallons of radioactive waste.<sup>[1]</sup> Waste was continuously added to the tanks from the site's opening in 1943 to the decommissioning of its last reactor in 1987.<sup>[2]</sup> The majority of the liquid waste has been extracted from the site's holding tanks, but all solid waste remains, which accounts for 27 million US gallons of the total waste volume.<sup>[1]</sup> An additional 2.8 million US gallons of liquid waste could not be extracted from the tanks. Removing the remaining waste at Hanford and processing it into a form that will be stable for long-term storage is significant logistical challenge.

Of Hanford's 177 tanks, 149 are single-shell steel containers ranging in capacity from 55,000 to 1,160,000 US gallons.<sup>[2]</sup> These tanks were designed to hold liquid waste for 10–20 years and have all exceeded their service lifetime, some several times over. While the majority of the liquid waste has been removed, the 2.8 million US gallons of liquid that remain continue to slowly leak through the corroded tank walls.<sup>[2]</sup> The environmental hazard posed by this leakage necessitates prompt measures to extract the Hanford waste from the on-site tanks.

Pumping liquid out of Hanford's tanks is straightforward compared to extracting solid waste. Removing the solid waste from these aging tanks requires knowing the size distribution of its particles.<sup>[3, 4]</sup> Solid waste is to be resuspended in liquid before being transported as a slurry through pipes, and the particle size distribution of the waste will affect the design dimensions of the piping and the requisite liquid flow rate.<sup>[5]</sup> If the pipes are too narrow or the flow rate too slow, solid waste settles to the bottom of the pipes and causes blockages – particle settling is especially

concerning for radioactive material because it creates highly localized radiation levels and can cause a critical mass to accumulate.<sup>[4]</sup>

Each tank contains a unique mixture of waste products, requiring the particle size distribution in each tank to be measured independently.<sup>[3, 5]</sup> Over the years, waste products from different nuclear reactions were mixed indiscriminately in the tanks.<sup>[3]</sup> These unregulated additions have resulted in uncontrolled chemical changes in the tanks, which along with internal temperature gradients and unmonitored phase separation, have created tank compositions that are difficult to predict without taking direct measurements.<sup>[3]</sup> Sampling the tanks for offline testing is challenging because of the waste's radioactivity, which makes samples difficult for human workers to interact with. These safety concerns make obtaining samples with the smallest possible sampling volume a priority; however, the tanks' large internal volumes and heterogeneous makeup (waste in the tanks is a mixture of sludge, saltcake, and supernatant fluid) make obtaining a proper representative sample difficult within practical sampling volume constraints.<sup>[6]</sup>

Due to the difficulty of predicting the composition of the wastes in the tanks and the difficulty of obtaining proper offline samples, it is necessary to determine the size distribution in the tanks via online means that can be applied *in situ*. Hanford's solid waste is thought to consist mostly of small dense particles and large soft agglomerates; however, the waste treatment design constraints and the measures to avoid settling are dictated by large hard agglomerates, which make up only a small percentage of the total waste volume.<sup>[7, 8]</sup> Closed-circuit particle grinders have been proposed to precisely control the particle size distribution of waste entering the waste treatment plant, but they too require a real-time sensor for measuring particle size to achieve size control.<sup>[5]</sup> Ultimately, an *in situ* method for particle sizing must handle a wide range of slurry densities and

compositions and must be able to detect small quantities of large particles, if it is to be practically applied to the Hanford waste.

Focused beam reflectance measurement (FBRM) is an industry-standard technology for online measurement of particles that possesses the desired sensitivity and flexibility for use in the Hanford waste. FBRM is sensitive to low concentrations of particles, and it is routinely used by researchers to track nucleation events in crystallization.<sup>[9-11]</sup> The manufacturer of FBRM, Mettler-Toledo, asserts that FBRM is functional in concentrated slurries or emulsions that are opaque.<sup>[12]</sup> FBRM is also capable of taking measurements more quickly (potentially one measurement every 2 seconds) than many competing technologies. *In situ* video microscopy, which is capable of recording images quickly, requires image analysis algorithms with long computation times to compute accurate particle sizes.<sup>[13-15]</sup>

While these advantages make FBRM an attractive option for use in the Hanford waste processing operations, adapting it for quantitative solid-phase monitoring requires additional numerical treatments to make practical use of the data it records, as FBRM does not directly measure particle size.<sup>[16]</sup> FBRM is traditionally used qualitatively, and a general means of applying its data to all particle systems does not currently exist. This thesis seeks to work towards a methodology for quantitatively interpreting FBRM data and applying it to size the Hanford waste, while also meeting the need for a method of monitoring a currently-used nonradioactive simulant.

## **1.2 Specific Motivation**

While *in situ* measurement of the Hanford waste's composition is a long-term goal salient to the cleanup procedures proposed by the Department of Energy (DOE), of more immediate concern are the mixing experiments currently occurring at the National Energy Technology

Laboratory (NETL). NETL is investigating the ability of pulse-jet mixers to resuspend the solids in the Hanford wastes.<sup>[17-19]</sup> Mixing the waste slurries to achieve complete solid suspension is necessary for transport through pipes, for the reasons discussed earlier in Section 1.1. Solid settling in mixing tanks is also unacceptable, as safety concerns would necessitate frequent down-time to manually clean the vessels used in the waste treatment plant.<sup>[4]</sup>

NETL uses a nonradioactive simulant designed to approximate the size distribution and density of the Hanford waste, but they do not currently possess a means of *in situ* particle monitoring.<sup>[20, 21]</sup> As a result, they must evaluate the quality of mixing with visual metrics like cloud height and off-bottom suspension, both of which are measured with the naked eye.<sup>[18]</sup> A drawback to this approach is that, for particles small enough to create a milky suspension, it is impossible to visually inspect a mixing tank beyond the very edges of its contents. This makes determining the slurry composition at the center of the tank impossible.

This objective of this thesis is the development of a method for monitoring the solid phase of the NETL's waste simulant in real-time. Using an empirical framework, this work uses FBRM to estimate the composition of the simulant slurry – specifically, the concentrations of the six particulate species that make up the NETL simulant are estimated to the best possible accuracy. Previous efforts for quantitative application of FBRM have focused on systems with a single particulate species; the methods described in this thesis can be generalized to any complex system containing diverse particles.

## CHAPTER 2. Background and Theory

### 2.1 FBRM Operating Principles

FBRM has been used for particulate monitoring since 1998.<sup>[22]</sup> The instrument uses light backscattering to estimate the quantity and size distribution of solid particles in a slurry. FBRM works by shining a laser beam into a mixture and rotating this laser in a circle, at a fixed velocity (shown in Figure 1A). When the laser beam crosses a solid particle, its light is scattered back towards the probe, where it is picked up by a detector.<sup>[12]</sup> The detector itself is part of the probe assembly, so only light that is scattered directly back towards the probe is measured. Backscattering continues until the laser moves off the particle, at which point the signal from the detector stops. Because the laser rotates at a fixed speed, the duration of each backscattering signal recorded by the detector can be converted into a chord — the length of the path taken by the laser across the particle surface (Figure 1B). These chords are counted and grouped according to their length to create a chord length histogram (CLH), which is a histogram that represents the distribution of particle sizes.

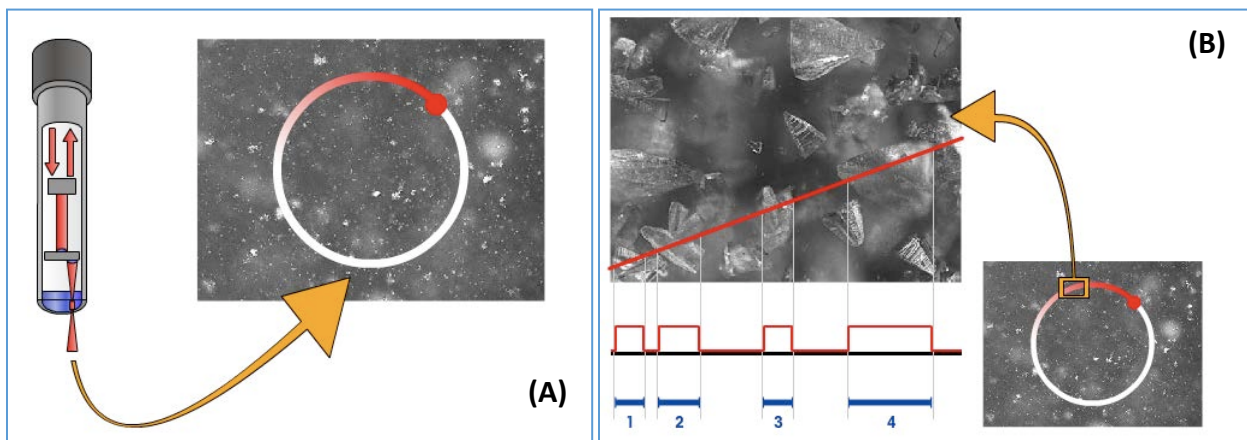


**Figure 1 – Schematic of FBRM probe operation. (A) The probe emits a laser that rotates at a fixed speed. (B) As the laser beam crosses particles, the probe detects the backscattered light. The duration of each pulse of backscattered light is translated into a chord length by multiplying by the laser rotation speed. Figure courtesy of Dan Griffin.**

The chord length histogram is a useful measure of many properties of the particulate system. The CLH has proven to be sensitive to changes in particle count,<sup>[23]</sup> average particle size,<sup>[24, 25]</sup> and particle shape.<sup>[26-28]</sup> However, the CLH is also influenced by many other factors. Some of these factors may not be related to solid phase transport, such as the index of refraction of the carrier fluid,<sup>[29, 30]</sup> the surface facets of the observed particles,<sup>[31]</sup> the opacity of the observed particles,<sup>[32]</sup> and the distance of the particles from the laser's focal point.<sup>[33]</sup> Distinguishing the properties of the CLH that are affected only by particle size is critical to any practical application of FBRM. For example, an observed decrease in the average chord length during a crystallization experiment might be the result of secondary nucleation. However, this same observation might be the result of crystal growth – large crystals are translucent and do not backscatter light as consistently as small crystals, which prevents FBRM from measuring the full crystal diameter.<sup>[34]</sup> Chord length is not an explicit measurement of particle size, and inferring particle size information from a chord length histogram requires considerable care.

## **2.2 Qualitative Uses of FBRM**

Due to the difficulty of quantitatively interpreting a CLH, FBRM is often used as a qualitative means of detecting major changes in a particulate system. While the shape of the CLH can change based on a number of optical factors related to the backscattering of the laser light, it is still sensitive to particle properties.

### *2.2.1 Qualitative Monitoring and Crystallization Control*

Based on the rate of change of certain chord count bins, it is possible to gain a qualitative understanding of crystallization kinetics. Increases in fine chord counts indicate that nucleation is occurring,<sup>[24, 35]</sup> and decreases in small counts accompanied by increases in larger chord counts

show crystal growth.<sup>[36]</sup> Using fine chord counts as a predictor for nucleation is a particularly useful qualitative measure, as the onset of nucleation can be measured for different solution concentrations to find the metastable zone limit.<sup>[11, 37-39]</sup> Additionally, monitoring nucleation is important in seeded crystallizations, in which the primary goal of seeding is to limit nucleation and force supersaturation to decrease via crystal growth alone.<sup>[39]</sup>

This application of FBRM to monitor the onset of nucleation is most commonly used to measure induction time<sup>[37, 38, 40]</sup> – which is the time it takes for crystals to nucleate when a solution is cooled under a linear temperature profile. By preparing several solutions at different concentrations, then lowering the temperature until fine counts are observed with FBRM, it is possible to plot a concentration vs. temperature curve that predicts when nucleation should occur at any solution concentration. The definition of ‘fine’ chord counts is arbitrary and is chosen by experimenters based on the particular system, as different crystal geometries will produce chord counts of differing lengths when primary nucleation occurs.<sup>[16]</sup> Plotting a curve showing the onset of nucleation at each concentration alongside the solubility curve shows the width of the metastable zone, where the solution is supersaturated but does not crystallize into a solid phase.

Adapting FBRM as a measure of nucleation behavior is also useful for crystallization control. While most measurements of induction time focus on characterizing primary nucleation behavior, FBRM is not limited to observing only primary nucleation events. Secondary nucleation, brought on by the presence of other crystals, is also observable by tracking changes in fine chord counts – FBRM can be used to monitor secondary nucleation and inform control policies that focus on growing large crystals.<sup>[41]</sup> Direct nucleation control (DNC)<sup>[41]</sup> considers FBRM as a measure of both types of nucleation to control a crystallization with a concentration profile that is within the metastable zone, keeping the nucleation rate approximately constant to drive the system towards

crystal growth.<sup>[10]</sup> DNC assumes that the number of chord counts recorded per second is an approximation of the total nucleation rate; by keeping the nucleation rate constant via cycles of heating and cooling (or solvent/antisolvent addition), large narrowly-distributed crystals can be produced with no *a priori* knowledge of the crystal system.<sup>[10, 42-44]</sup>

In addition to crystallization control, the real-time monitoring offered by FBRM allows for the implementation of alternative crystallization protocols that yield large average crystal sizes. Chew et al. formulated a method to reproducibly create crystals with desirable sizes by first cooling a saturated salt solution until nucleation is detected, then stabilizing the temperature and heating the mixture to dissolve small crystals.<sup>[45]</sup> The crystallizer is heated until the CLH shows a targeted coefficient of variation value (the ratio of the CLH standard deviation to the mean chord length), effectively creating seed crystals *in situ*.<sup>[45]</sup> Cooling again from this point to the target crystal yield produces crystals with a consistent size distribution. This approach, known as internal seeding, can be augmented with DNC in the initial cooling/heating phase to produce yet larger seed crystals.<sup>[46]</sup> Internal seeding crystallization can be further improved by implementing supersaturation control instead of linear cooling once the seed crystals are formed – cooling while maintaining a constant supersaturation value prioritizes growth and increases the final crystal size.<sup>[47]</sup> While none of these techniques make full quantitative use of the CLH, all are made possible by the FBRM's ability to rapidly monitor solid phase changes.

### 2.2.2 *Monitoring Polymorphic Transitions*

Because changes in particle shape affect the size and shape of the CLH, FBRM can be used to qualitatively monitor polymorphic transitions of crystals. Figure 2 shows the two methods researchers use to evaluate changes in particle shape: plots of the entire chord length range, and plots of the counts in specific regions of the CLH over time.

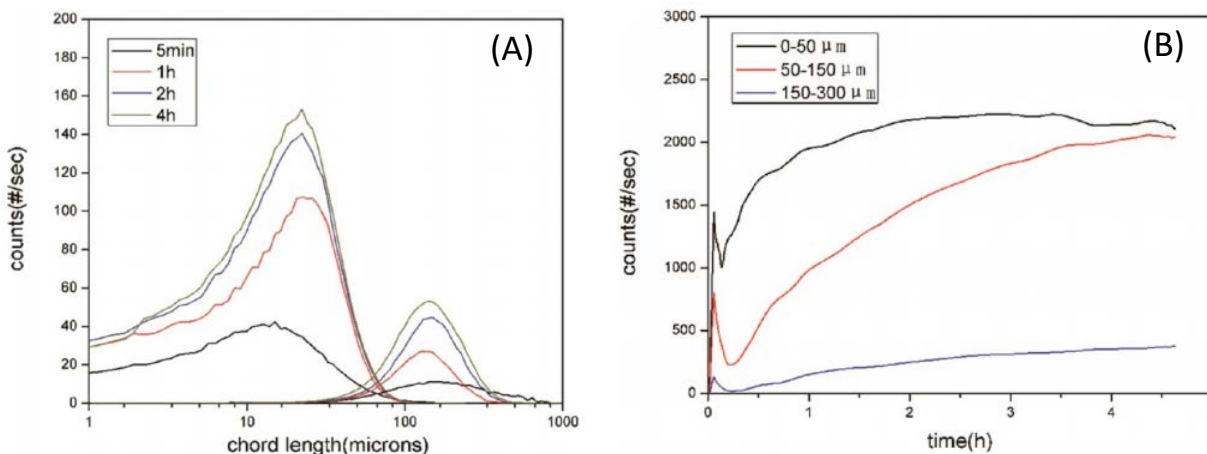


**Figure 2 – FBRM visualization of imidacloprid polymorphic transition from Form II (needle-like) to Form I (flaky). (A) Unweighted (left curves) and square-weighted (right curves) CLHs, plotted at different times during the crystallization experiment. (B) Groupings of fine counts (0-50  $\mu\text{m}$ ), medium counts (50-150  $\mu\text{m}$ ), and coarse counts (150-300  $\mu\text{m}$ ) at every time point during the crystallization experiment. Reproduced with permission from Zhao et al.<sup>[36]</sup>**

Figure 2A shows the chord counts measured by FBRM in a crystallization experiment for imidacloprid where a polymorphic transition from Form II to Form I is observed. The figure shows how the characteristic shape of the CLH can change as a particle species, in this case Form II imidacloprid, experiences a corresponding shape change. It should be noted that the time resolution shown in Figure 2A is somewhat coarse to avoid a dense and unreadable plot. To increase the time resolution while still showing qualitative changes in particle shape, the CLH is separated into large bins and summed, as in Figure 2B. In this plot, the changes of the fine, medium, and coarse counts over time can be tracked more easily. In Figure 2B, it can be seen that the rapid dissolution of crystals, which are assumed to be in Form II, occurs after 5 minutes, followed by the nucleation of new crystals, which are assumed to be Form I. Such an observation cannot be made from Figure 2A, which shows the CLH at infrequent time points. The two types of plots shown and discussed above are often used by researchers for CLH analysis to monitor and understand polymorphic transitions.<sup>[26-28, 36, 48]</sup>

Because the shape of the CLH is sensitive to particle properties unrelated to shape, FBRM data is often corroborated with alternative monitoring instruments to insure that observed CLH changes correspond with changes in crystal shape. Offline microscopy can be used to verify particle shape, provided that it is possible to take representative samples during the crystallization experiment.<sup>[28]</sup> Particle vision measurement (PVM) is another common means of visually inspecting particle shape, as it allows for real time imaging of the particle system without the need for sampling, albeit with less resolution than offline microscopes.<sup>[26, 27, 36, 48]</sup> *In situ* Raman spectroscopy is another technique that is sensitive to real time changes in particle shape, and it has been used alongside FBRM for monitoring the polymorphic transition of D-mannitol.<sup>[37]</sup> All of these techniques are capable of providing a second source of shape monitoring to verify observations made with FBRM.

## 2.3 Quantitatively Relating CLH to PSD

### 2.3.1 Linear Model

Transforming a given CLH into a particle size distribution (PSD) and vice versa is possible if enough information about the particle system is known. For each particle scanned by the FBRM laser, the length of the chord it generates depends on the particle's shape, rotation, and position.<sup>[22,</sup>  
<sup>33]</sup> A linear model can be used to combine the CLHs expected from each bin in the PSD, and thereby predict what the CLH of a particular batch of particles should look like. The relationship between chord length and particle size distributions can be modeled by the following linear correlation:

$$c = Ux \tag{2.1}$$

$$x \in \mathbb{R}^n, c \in \mathbb{R}^m, U \in \mathbb{R}^{m \times n}$$

where  $c$  is the CLH in bins from  $l_1 \dots l_{m+1}$  with  $m$  being the total number of chord length bins,  $x$  is the discretized PSD in bins from  $s_1 \dots s_{n+1}$  with  $n$  being the total number of particle size bins (elements in  $x$  have units of number of crystals per unit volume), and each element  $U_{ij}$  is the probability that a particle of size  $s_i$  generates a chord between lengths  $l_j$  and  $l_{j+1}$ .<sup>[22, 49]</sup>

The linear model makes two critical assumptions about the behavior of the CLH and the behavior of the particulate species. First, the chord counts are proportional to the number of particles. Under this assumption, the CLH produced by two particles of the same size must equate to double the single particle's CLH<sup>[22]</sup>. If this assumption is invalid, multiplying an element of the PSD  $x_i$  by its corresponding column in  $U$  would not accurately recreate the CLH of these particles. Second, the CLHs of different-size particles must be additive — the CLH produced by two particles of different sizes must be equal to the superposition of the individual CLHs of those particles.

A model that assumes a linear relationship between chord counts and particle counts has been shown to be useful for crystallization control.<sup>[50]</sup> Even when FBRM is not used to directly measure particle size, a particle count estimate can be combined with other process analytical techniques to characterize a solid-liquid suspension, as was discussed in Section 2.2.1. The linear relationship between CLHs and particle size distributions generally holds true at low solid volume fractions; this relationship grows gradually more nonlinear as solids fraction increases, eventually reaching a saturation point where the addition of more solids to the mixture does not cause a chord count increase.<sup>[25]</sup> This saturation of the counts is thought to occur because of the increasing probability of overlapping particles as the suspension density increases.<sup>[51]</sup> FBRM will count a pair of overlapping particles only once, leading to decreased counts per suspended particle. The point at which linearity breaks down is unique to each particle species<sup>[52]</sup> and dependent on the particle

size.<sup>[25]</sup> Figure 3 shows total chord counts against solid fraction for calcite particles. It can be seen that the slope of chord counts decreases as the solid fraction increases, which indicates the saturation point's dependence on particle size, depicting the chord counts per solid fraction curves for sieved fractions of calcite.

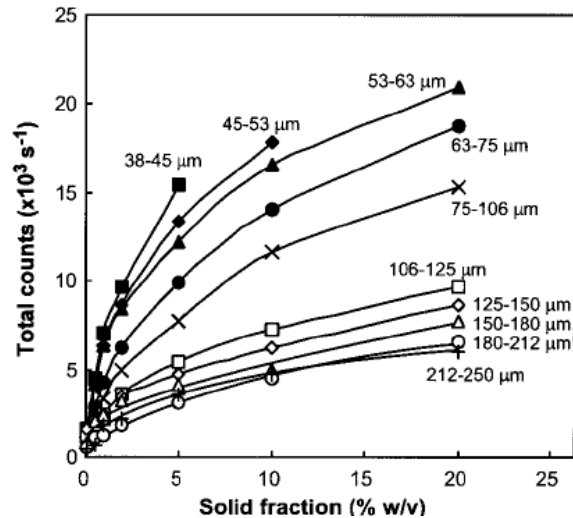


Figure 3 – Counts versus solid fraction for different size ranges of calcite particles, reproduced with permission from Heath et al.<sup>[25]</sup>

For the calcite fractions shown in Figure 3, the counts produced by large particles saturate more slowly than the counts produced by small particles. While the curves of same-size particles of different species saturate at different rates, size always influences the saturation rate in a predictable manner.<sup>[52]</sup> Larger particles produce fewer counts per unit mass than small particles, and their chord count plots saturate more slowly than small particles — Figure 3 shows both of these points.

The second assumption made by the linear model is that when particles from two size bins in the PSD are mixed, their CLH fingerprints must be additive. In a situation where there are two particles of different sizes in suspension, this assumption states that the CLH produced by these particles must still equate to the superposition of the particles' individual CLHs.<sup>[22]</sup> This

assumption is what facilitates a matrix transformation between the CLH and the PSD. Tan *et al.* verified this assumption for the simple system of polystyrene spheres in deionized water; however, it is not guaranteed to hold when differently shaped particles are observed together, when particle shapes are more complex than spheres, or when the particles interact physically with each other (i.e. agglomeration or aggregation).<sup>[34]</sup>

## 2.3.2 *First-principles Approaches*

### 2.3.2.1 Geometric Modeling

The elements of  $U$  have been estimated via numerous first-principles approaches in previous research. First-principles methods developed before 2008 neglected details of the light backscattering and considered the FBRM system from a purely geometric perspective.<sup>[29]</sup> Purely geometric models assumed that the width of the focused laser beam is effectively zero. These models assumed that the reflection of light is not impacted by 1) the distance between the particles and the laser focal point, 2) the refractive index of the suspension medium, or 3) the overlapping of particles in dense slurries.<sup>[34]</sup> Geometric models also assume that aspects of the particle surface such as curvature, smoothness, and translucence do not impede the detection of light backscattered into the probe.<sup>[53, 54]</sup>

The most common geometric method for this calculation assumes an ellipsoidal cross-section for all particles.<sup>[22, 55-57]</sup> Assuming that the particles being observed are spherical makes the model formulation simpler because spheres' 2D cross-sections are the same regardless of rotation. Such geometric models based on spheres have been successfully applied to polymer systems and slurries of ground minerals.<sup>[25, 58]</sup> However, the spherical assumption does not produce accurate results for most crystal species, which have well-defined facets.

For particles with ideal light reflection characteristics, assuming that particles have an ellipsoidal cross-section can approximate the correlation between the particles' size and the CLH obtained from FBRM .<sup>[56]</sup> An ellipse is defined by its semi-minor and semi-major axes  $a$  and  $b$  as such:

$$a = \sqrt{\frac{s^2}{4r}}; \quad b = ra \quad (2.2)$$

where  $s$  is the particle's equivalent spherical diameter and  $r$  is the aspect ratio between the major and minor axes. With these dimensions, it is possible to calculate the probability  $p$  of cutting a chord between lengths  $l_j$  and  $l_{j+1}$  given a fixed angle  $\alpha$  — the angle is calculated by assuming that the laser is incident at the particle's edge on the minor axis,

$$p(l_j, \alpha) = 2 \left( \frac{f(l_j, \alpha) - f(l_{j+1}, \alpha)}{f(0, \alpha)} \right); \quad f = 2d \cos(\alpha) \quad (2.3)$$

where  $d$  is the shortest distance between the particle's midpoint and the chord. Integrating the above probability equation from  $\alpha = 0$  to  $\pi$  gives the full probability of recording this chord length for a particle of equivalent spherical diameter  $s_i$ . From this probability, we construct a matrix  $U$ .<sup>[57]</sup>

$$U = \begin{bmatrix} p(s_1, l_1) & p(s_2, l_1) & \dots & p(s_n, l_1) \\ p(s_1, l_2) & p(s_2, l_2) & & \vdots \\ \vdots & & \ddots & \\ p(s_1, l_m) & \dots & & p(s_m, l_n) \end{bmatrix} \quad (2.4)$$

This model is effective for particles with ideal reflection characteristics, but it deviates significantly from real data in the majority of cases. Particles with smooth surfaces backscatter incident light in a primarily specular fashion (meaning that the majority of incident light is reflected at the incoming light's angle of incidence) – this causes most of the laser light contacting

the particle to be scattered away from the detector, which is located in the probe along with the source. Thus, fewer chord counts are generated, compared to the geometric model's prediction for like-sized particles with ideal reflection characteristics.<sup>[29, 30, 59]</sup>

Geometric models also fail to describe the behavior of translucent particles under FBRM monitoring. Translucent particles allow a large percentage of incoming light to pass directly through them without registering a backscattering signal. Only the edges of these particles backscatter a large enough quantity of the laser beam to register a chord count – this edge detection results in a phenomenon known as chord splitting, where a large particle will produce two or more short chord counts instead of one long count as it is encountered by the laser.<sup>[22, 29]</sup> Figure 4 is a photomicrograph of a glass bead, which gives a visual explanation of chord splitting using the spherical glass bead as an example to illustrate how the dark edges of a translucent object are converted into chords.

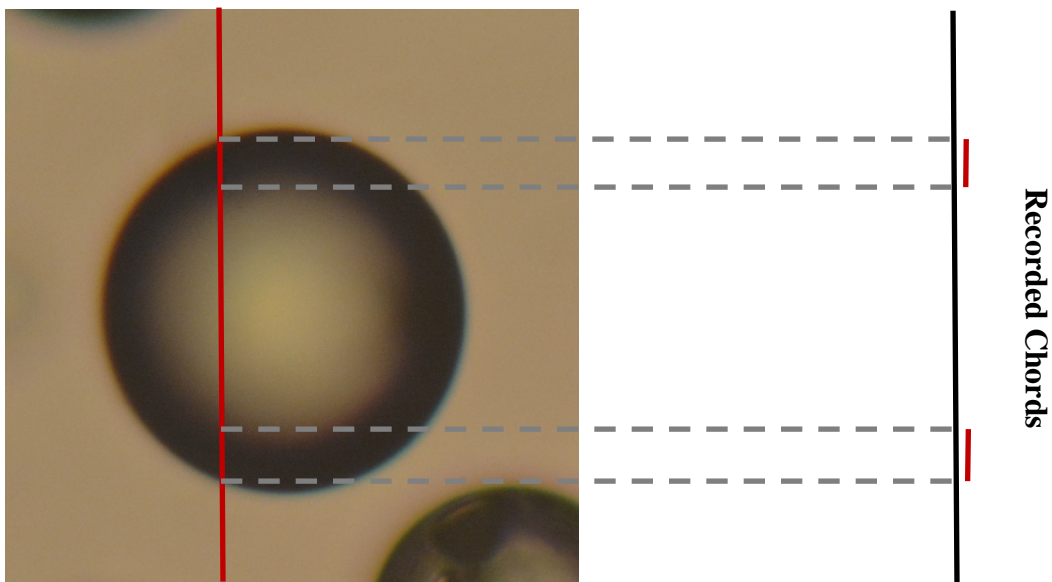


**Figure 4 – Illustration of chord splitting on a photomicrograph of a 50  $\mu\text{m}$  glass bead. The red line through the image represents the theoretical travel path of an FBRM laser. Dashed lines are drawn to show where the laser intersects with the dark parts of the particle.**

The photomicrograph in Figure 4 was taken using transmitted light, so the dark areas on the particle are regions where the light was reflected or scattered and did not reach the microscope eyepiece. An FBRM laser incident on this glass bead's surface would be reflected in the same way: only the edges facilitate enough backscattering to register a chord count, while the clear center allows the majority of the laser's intensity to pass through it, hence splitting one chord into two smaller chords. Additionally, particles with smooth surfaces like the glass bead in Figure 4 may scatter a yet smaller fraction of light back towards the detector when illuminated, shortening the chords further or preventing them from being recorded at all.<sup>[29, 30]</sup> Modern FBRM firmware features built-in edge detection to handle inconsistent scattering and increase the chance that the full width is measured,<sup>[60]</sup> but no means of signal processing can achieve a perfect solution to chord splitting. If the FBRM firmware is configured to convert large particle edges into single chords, it also concatenates chords generated by closely spaced small particles into larger chords.

#### 2.3.2.2 Modeling Backscattering

Because geometric modeling is only effective for the small group of particles that backscatter light uniformly, the logical next step to improve the accuracy of first-principles models is including light reflection properties in the model formulation. Two papers by Kail *et al.* proposed a model that exhaustively simulated the optical mechanisms of an FBRM probe – in their case, the Lasentec D600L.<sup>[29, 30]</sup> Unlike the geometric model, this thorough approach modeled the changes in the CLH that occur due to laser beam broadening, intensity loss through the liquid phase, multi-directional backscattering, and changing distance between particles and the laser focal point. By calculating both external scattering efficiency (the percentage of the light incident on the particle that is scattered back to the probe) and internal scattering efficiency (the total percentage of emitted light that reaches the detector inside the probe), the optical model could predict the FBRM probe's

measured light intensity profile from a population of particles.<sup>[29]</sup> By applying a chord discrimination algorithm to convert the light intensity signal to measured chords, the CLH of a known particle population could be estimated – unlike the geometric model, this model correctly predicted the oversizing of small particles due to beam broadening and the chord splitting behavior exhibited by large particles.<sup>[30]</sup>

This type of rigorous optical modeling was shown to be capable of accurately estimating the CLH produced during the crystallization of DL-threonine in water,<sup>[61]</sup> but rigorous first-principles modeling is unsuitable for use in a nuclear waste system for several reasons. The principal difficulty in adapting this model for nuclear waste, or for a nuclear waste simulant, lies in the model's requisite input information. A model capable of describing the light scattering behavior of large (>30  $\mu\text{m}$ ) particles requires knowledge of the particles' surface orientation, surface texture, and transparency;<sup>[29]</sup> for a mixture of multiple particle species, this information must be input for every species, and the FBRM laser's interaction with each species must be specifically modeled. Because the optical model developed by Kail *et al.* also explicitly modeled the internal optics of the FBRM probe, it may not be generalizable to FBRM hardware that differs from the hardware used in Kail's experiments. The quantity of *a priori* information needed to accurately apply first-principles optical models to multi-particle systems limits their potential. As an alternative to rigorously calculating the elements of the CLH-PSD transformation matrix  $U$ , they can be measured from data to construct an empirical model.

### 2.3.3 Empirical Approaches

The first-principles models described in Section 2.3.2 allow for accurate estimates of particle size for well-characterized particle systems. However, to accurately predict FBRM data, first-principles models require enough knowledge about the particle system being studied and

enough system-specific assumptions that they are difficult to generalize to multiple types of particles.<sup>[16, 34]</sup> Nuclear waste mixtures are too complex to feasibly apply these models, containing a wide range of particle sizes and materials;<sup>[3, 8]</sup> even waste simulants, designed to approximate the characteristics of nuclear waste with reduced complexity, contain multiple components that would be difficult to size accurately with FBRM.<sup>[20, 21]</sup>

Given the practical constraints that limit first-principles calculation of  $U$ , empirically populating the linear model is an attractive alternative to first-principles approaches. Using an empirical approach allows the system's light reflection characteristics to be treated as a black box via the incorporation of experimental data. Particularly for mixtures of several particle shapes, empirical modeling allows the complex interactions between particles to be modeled without exhaustive *a priori* system characterization. Empirical modeling still requires extensive data collection, but empirical models can be informed by basic experiments performed with just the FBRM equipment itself. It is for this reason that empirical modeling was chosen for the system examined in this thesis.

Several empirical treatments for interpreting FBRM data have already been formulated by researchers. A common approach focuses on correlating the moments of the CLH with aspects of the particle size distribution measured through other means, essentially treating the CLH itself as a gray box and examining only the moments that change with practically useful quantities.<sup>[62]</sup> The first moment of the CLH has been previously correlated with average particle size,<sup>[52, 63]</sup> and CLH moments have been used to calculate kinetic parameters for pharmaceutical crystallizations;<sup>[38]</sup> however, correlations between CLH moments and PSD characteristics that are generalizable to multiple particulate systems have yet to be found.<sup>[64]</sup>

Li *et al.* proposed an empirical framework using the same linear model structure described in Section 2.3.1., which effectively estimated the size of a population of paracetamol crystals.<sup>[31]</sup> This framework proposed using the same matrix transformation shown in Equation 2.1, but instead populating it with ‘fingerprint’ CLHs recorded experimentally for each PSD element  $x_i$ .<sup>[31, 65]</sup> The columns of matrix  $U$  are populated with FBRM data representative of each size range, divided by the number of particles used in the measurement of the fingerprint:

$$c = [u_1 \quad u_2 \quad \dots \quad u_n]x$$

$$u_i \in \mathbb{R}^m \tag{2.5}$$

for  $n$  bins in the particle size distribution. Equation 2.5 is the same as Equation 2.1, but it is expanded to show the individual columns of the matrix  $U$ . Here,  $u_i$  is defined as a fingerprint for population  $i$  with abundance  $x_i$ . In this way, the PSD of any FBRM data set is estimated as the linear combination of fingerprints that best approximates the data.

In Equation 2.1, by choosing the vector  $x$  so that only one element is nonzero (i.e.  $x = (0, \dots, 0, x_i, 0, \dots, 0)$ ), the resulting CLH  $c$  from this particle size distribution is given by  $x_i u_i$ . A column  $u_i$  of  $U$  is equivalent to the CLH that the model predicts for its corresponding bin  $x_i$  in the particle size distribution. Therefore, individual measurements taken from particles in each bin of  $x$  can be used to populate  $U$  in lieu of accurate parameters determined by first-principles. In fact, it is not necessary that  $x$  represents the abundance in monodisperse bins defined by size. The bins in  $x$  could be well-characterized distributions and might not be monodisperse.

This model was validated using paracetamol crystals in water and was able to accurately reconstruct CLHs measured experimentally from crystals between 20 and 500  $\mu\text{m}$  in length.<sup>[31]</sup> The resolution of the PSD is limited by the obtainable samples of the target particles – because the

particles in each size bin of the PSD must have their CLHs independently recorded, it must be possible to obtain samples of those particles to measure with FBRM. For crystallizations, the PSD resolution will likely be limited by the mesh spacing in standard sieve trays; additionally, crystals that are difficult to accurately separate via sieving (such as needle-like crystals) will likewise be difficult to size using Li's method. Despite this limitation, Li's empirical approach yields results with shorter computational times than alternative sizing means such as *in situ* image analysis, and it requires less *a priori* knowledge of the particle system than first-principles FBRM models based on light scattering.<sup>[29, 30]</sup>

## 2.4 Regressing PSD from CLH

Constructing the matrix  $U$  allows for the estimation of a particulate slurry's CLH if its size distribution is known. However, the more practical application is working the problem in reverse, where a measured CLH is used to estimate the PSD of an unknown sample. To realize such an application, an inverse problem, or estimation problem, must be solved. This estimation is nontrivial because of the nonuniqueness of FBRM measurements (multiple PSD's can map onto the same CLH). If the inverse solution  $Ux = c$  to Equation 2.1 is not unique, additional assumptions must be made to formulate a solution that is well-defined. Even with relatively simple geometric modeling such as the formulation described in the Section 2.3.2.1, the matrix  $U$  is generally ill-conditioned for non-spherical particles.<sup>[66]</sup> When  $U$  is ill-conditioned, noise in the CLH measurement may create artifacts in the estimated PSD. These complications often preclude simple linear regression from being used to solve the inverse problem, as small deviations due to noise will have huge effects on the estimated PSD.

Many approaches to solving the inverse CLH-PSD problem add additional assumptions or constraints to simplify the problem. Worlitschek et al. used a method called projections onto convex sets, where the PSD vector  $x$  is projected onto all the sets associated with the chosen constraints (i.e.  $x \geq 0$ ) before being solved iteratively, to back out particle size from noisy FBRM measurements of ceramic spheres.<sup>[67]</sup> Adding a nonnegativity constraint to conventional least-squares regression can suppress some oscillations in the solution, and it has been successfully applied to static mixtures of opaque particles<sup>[56]</sup> and to paracetamol crystallizations.<sup>[68]</sup> Where this constraint alone is insufficient, assumptions can be made about the shape of the PSD solution; for example, the PSD can be forced to conform to a certain smoothness constraint, in a process called regularization.<sup>[31, 57]</sup> If particles are being monitored in a flow environment, the particle orientation bias induced by the fluid flow can be used to constrain the PSD.<sup>[69]</sup> It has also been shown that principal component analysis (PCA) is capable of calculating the PSD from FBRM measurements.<sup>[66]</sup> PCA allows a solution to be computed without non-physical constraints (such as regularization, which leads to an incorrect solution if the PSD is not smooth).

There are several promising approaches for converting chord length measurements into more practically useful information. The first-principles approach described by Kail *et al.* is capable, but the complexity of the simulant mixture used in this study necessitates an empirical approach. This thesis makes use of the empirical framework developed by Li *et al.* instead because it is simple to implement and has shown to be effective when applied to paracetamol crystals.<sup>[31]</sup> Additionally, Li's model can be adapted to estimate composition instead of particle size distribution, which will be discussed more in the next chapter.

## CHAPTER 3. Methods

### 3.1 Equipment Setup

Our crystallization lab is equipped with an OptiMax™ workstation made by Mettler-Toledo, depicted in Figure 5.

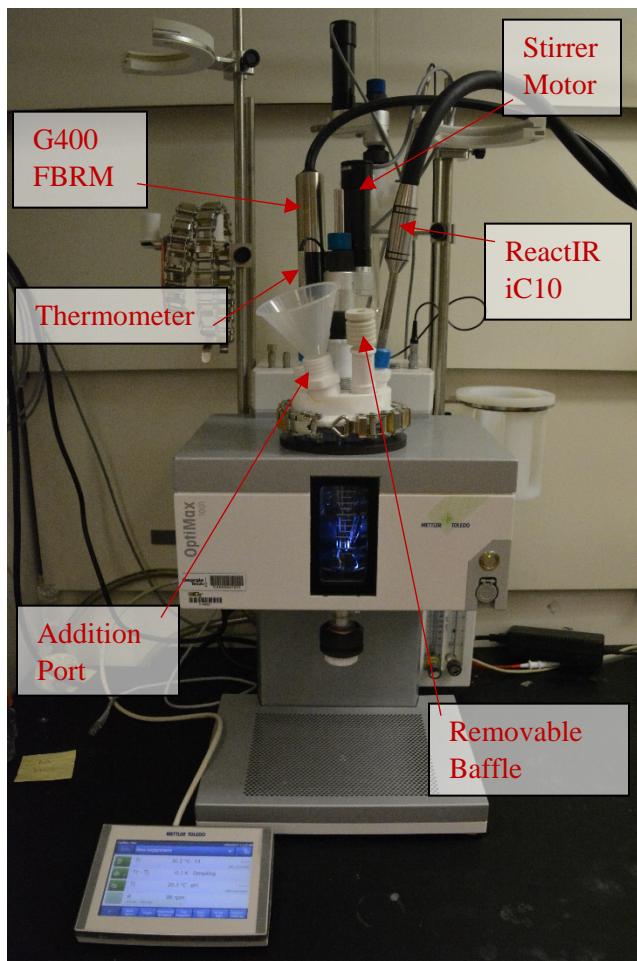


Figure 5 – OptiMax™ system with attached probes

The workstation contains a 1000 mL crystallizer and is capable of controlling temperature and agitation. The crystallizer includes customizable ports for various instruments, which in this case have been populated with an FBRM probe, an ATR-FTIR probe, and a removable baffle. ATR-FTIR is not used in these experiments, but along with the baffle, it influences the fluid flow

in the system, and thus also the size and shape of any measured CLHs. Data from all instruments is gathered by Mettler-Toledo's iControl™ software, where it can be further interfaced with MATLAB and Microsoft Excel. This interfacing feature can be used to estimate particle distribution in real time, using any of the models discussed in Chapter 2, and display this distribution on screen. iControl™ also records and saves all data from the OptiMax™ in its own file format, a capability which was used extensively in this thesis.

### **3.2 Solid-phase Monitoring**

A Mettler-Toledo G400 FBRM system records the CLH of the particles in the OptiMax™ and communicates it to iControl™, the crystallizer's software suite. The G400 uses a laser wavelength of 750 nm and moves the laser at a speed of 2 m/s. Mettler-Toledo's icFBRM™ software natively offers length-square weighting in addition to the unweighted chord length data. Weighting the CLD by the squared chord length of each bin is typically more useful for measuring large particles because it accentuates the counts from particles with large cross-sectional areas. Unweighted counts, on the other hand, depend more on the properties of small particles that have a high number density. Additional weighting of the distribution can be applied manually if desired (for example, past studies have examined volumetrically-weighted CLHs<sup>[22, 23]</sup>), but this capability is not used in this thesis.

### **3.3 Six-component Waste Simulant**

This work employs a simulant for nuclear waste due to the logistical difficulties of transporting and handling radioactive material. Previous simulants were composed of glass beads, with added dense components to simulate concentration spikes.<sup>[70]</sup> The current simulant consists

of six components that, when mixed together in the ratios listed in Table 1, approximate the density and particle size distribution of the Hanford waste.<sup>[71]</sup>

**Table 1 – Department of Energy (DOE) waste simulant. Solids are mixed with deionized water to achieve a total solids content of 12 wt%. Multiplying this solid fraction by the percentages in the third row yields the final amounts in the fourth row.**

	SiC	Tungsten	Glass	Al <sub>2</sub> O <sub>3</sub>	SiO <sub>2</sub>	Glass
Size [μm]	1-10	10-19	45-90	210-400	297-841	841-1190
Density [g/ml]	3.2	9.6	2.5	3.9	2.65	2.5
Solid Composition [wt%]	52.0	4.0	38.0	3.5	1.0	1.5
Composition with Water [wt%]	6.24	0.48	4.56	0.42	0.12	0.18

All solids were packaged by and received directly from the National Energy Technology Laboratory (NETL). Both sizes of glass beads were supplied by Potters Industries LLC, the silicon carbide (size F1000) was procured from Industrial Supply Inc., the tungsten shavings were supplied by Buffalo Tungsten, the alumina was supplied by Kramer Industries Inc., and the silica particles (sand) were supplied by U.S. Silica.

To form the waste simulant, these solids were mixed with deionized water to form a slurry with a total solids fraction of 12% by weight. We chose this concentration of solids because it was the upper limit used by NETL in their experiments. We also performed additional experiments at low solids fractions to assess the lower limits of detectability – below a minimum number density, particles do not generate enough counts to be indistinguishable from noise.

The simulant species are diverse particles, varying significantly in both density (ranging from 2.5 g/ml to 9.6 g/ml) and morphology. Figure 6 shows micrographs taken of each component, with scale bars to illustrate their sizes.

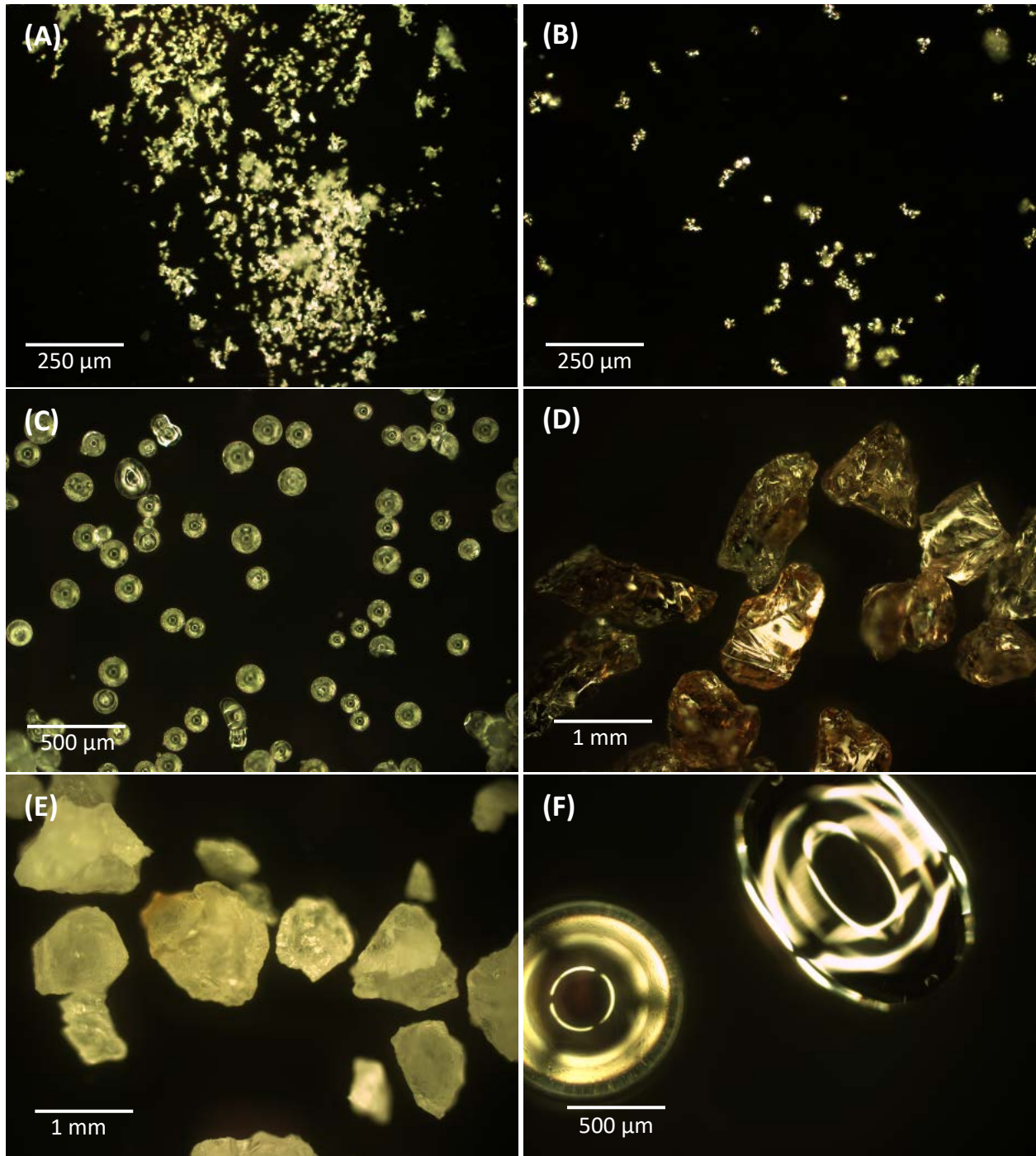


**Figure 6 – Micrographs of the six simulant components. (A) Silicon carbide, (B) tungsten alloy, (C) 45-90  $\mu\text{m}$  soda-lime glass beads, (D) alumina ( $\text{Al}_2\text{O}_2$ ), (E) sand ( $\text{SiO}_2$ ), (F) 841-1190  $\mu\text{m}$  soda-lime glass beads.**

The micrographs in Figure 6 employ forward lighting, as they would appear dark and featureless under traditional back lighting. Both groupings of glass microspheres have similar properties, but backscatter light differently due to their sizes. The small spheres, with their

increased surface curvature, allow less light to pass directly through compared to their large counterparts – this optical behavior is visible on a macroscopic scale as well, where the small spheres appear to the naked eye as a white powder. Conversely, the large spheres appear to the naked eye as clearly translucent beads. Silicon carbide and tungsten are both small metallic particles with reflective surfaces. Alumina and silica are both large and appear crystal-like, but alumina is less consistently reflective than the other non-glass particles. The micrograph of alumina in Figure 6D shows that the majority of its surface reflects light in a specular manner, with dark brown patches that reflect light poorly in any direction (silica, by contrast, is consistently bright and diffusively reflective).

### **3.4 Experimental Methods**

To obtain the chord length fingerprints used in the empirical model, each of the six components were placed in water, agitated at 400 RPM, and monitored with FBRM. A constant volume of water, 500 mL, was used in each experiment to guarantee total immersion of the probe in the slurry. The FBRM G400 system offers two algorithms for calculating chords from the raw backscattering signal recorded by the probe – these are called the primary and macro modes, intended for emphasizing the signals from small and large particles, respectively. The component CLHs were recorded with the primary chord discrimination mode, which despite its intended purpose of emphasizing the contribution of small particles, produced the most counts from the large components relative to the small components. Histograms were recorded using a fifteen-second measurement interval. Although individual measurements are taken every fifteen seconds, readings were averaged over longer time intervals to obtain smooth histograms that were representative of the components' actual CLHs. For the three small components (silicon carbide, tungsten, and small glass spheres), fingerprints were taken at their concentrations in the complete

simulant, listed in the fourth row of Table 1. The three large components (alumina, silica, and 841-1190  $\mu\text{m}$  glass spheres) are too dilute in the simulant itself to produce smooth fingerprints, so their concentrations were increased to 2.91% by mass to provide more total counts, and thus a smoother overall CLH. This new concentration was roughly an order of magnitude greater than the large component concentrations used in the simulant, so it was necessary to later evaluate the chord count linearity up to this increased concentration.

The same experimental procedures used in recording the fingerprints were used to take validation data sets: measurements of component combinations used to test the model's ability to estimate their composition. The stir speed and liquid volume were kept constant to prevent the relationship between chord counts and particle counts from changing.

### **3.5 Computational Methods**

Employing the empirical model to estimate composition from a measured CLH requires some form of regression. This work uses simple constrained least-squares regression, which can find a unique solution for this six-component system. Adding more components to the mixture would increase the complexity of the system and would increase the likelihood that the regression's solution would be non-unique. This work uses only a non-negativity constraint to compute the composition estimate, and the effectiveness of this approach will be evaluated in the next chapter.

Estimation of the six component masses from the measured CLH is challenging because the large components produce significantly fewer chord counts per unit mass than the small components. Because their fingerprints are so small, it is easy for any regression algorithm to add them to the composition estimates in large amounts to affect a small increase in the goodness of

fit. To avoid overfitting, a parameter selection step was added to the model in order to choose the smallest possible number of fingerprints that can create a good approximation of the data. This step considers every possible combination of the six fingerprints and calculates the Akaike information criterion (AIC) for the model containing that subset of fingerprints. The formula for the AIC is

$$AIC = 2F + 2\ln(\hat{L}) \quad (3.1)$$

where  $F$  is the number of fingerprints considered and  $\ln(\hat{L})$  is the optimized loglikelihood for the model and the given set of data. Equation 3.1 can also be written in terms of the mean squared error (sum squared error divided by the number of chord length bins).

$$AIC = 2F - m(\ln(2\pi MSE) + 1) \quad (3.2)$$

The symbol  $F$  in Equation 3.2 is the same as the  $F$  used in Equation 3.1,  $MSE$  represents the mean squared error, and  $m$  is the number of bins in the chord length distribution. The fingerprint set with the lowest AIC has the best balance between model simplicity and goodness of fit, and is chosen for the final composition estimation.

To find the number of possible combinations of components, one must calculate the binomial coefficient for every value of  $F$ . The formula for the binomial coefficient is given by Equation 3.3.

$$\binom{n}{F} = \frac{n!}{F!(n-F)!} \quad (3.3)$$

For the six components in the simulant, calculating  $n$  choose  $F$  for every possible value of  $F$  yields 63 combinations of components. MATLAB includes a function `nchoosek()` that automatically

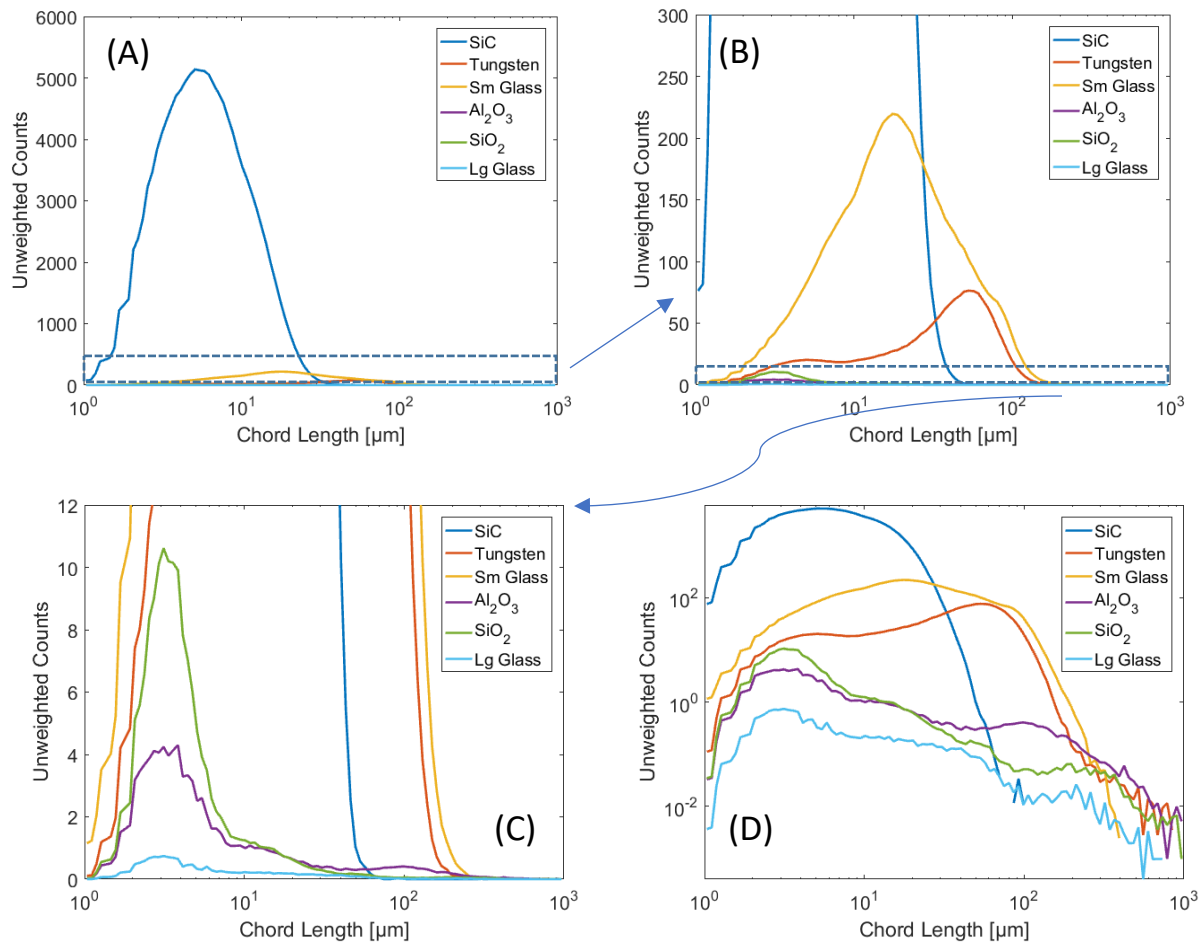
calculates the binomial coefficient and prints the enumerated combinations to a matrix, which is used to select the components for each AIC calculation.

Previous work has shown that chord counts shorter than 30  $\mu\text{m}$  vary more between experiments than counts in higher bin numbers.<sup>[31]</sup> They are more prone to noise and do not always increase linearly as particles are added to the system, making them less useful for quantitation. These counts may still contain valuable information, and so their adherence to the assumptions of the linear model is examined in Chapter 4 to make an informed decision with respect to the simulant used in this work.

## CHAPTER 4. Results & Discussion

### 4.1 Component Fingerprints

In order for FBRM to distinguish between two particle species, they must have distinctly shaped chord length histograms. The three smallest components in the Hanford simulant behave uniquely when observed with FBRM, although some share similar characteristics.



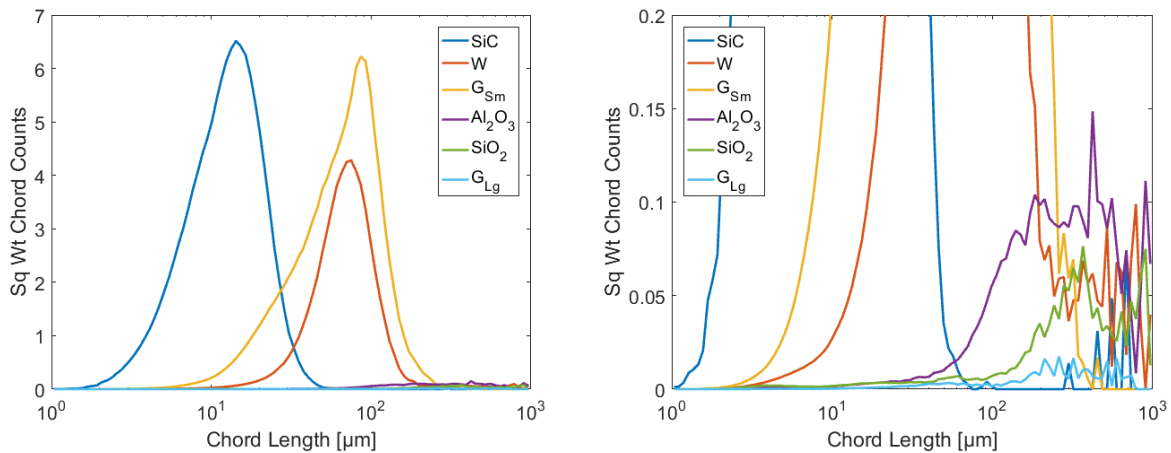
**Figure 7 – FBRM histograms for all six simulant components. The weight fractions of the three smallest components used to create these fingerprints are given in Table 1. The large components used 15 g of solid material in 500 mL of deionized water to produce more chord counts. (A) All components plotted on an axis automatically sized for SiC, showing the disparity in total counts between SiC and the other components. (B) Component histograms, zoomed in to show the shapes of tungsten and small glass spheres. (C) Component histograms, zoomed in to show the shapes of the three largest components. (D) Component histograms plotted on a logarithmic y-axis.**

Figure 7 shows the components' chord length histograms plotted together, at various levels of zoom. The three plots in this figure show the different shapes and sizes of the CLH for these simulant components. Figure 7A illustrates the peak height difference between the SiC CLH and the other five components. This difference was expected, as it is the dominant component in terms of both weight percent and number density. However, the difference in counts was so significant that the other components were difficult to detect while SiC was present.

Figure 7B, zoomed to show the CLH shapes of the other components more effectively, shows a similar count difference between the three smallest components (SiC, tungsten, and small glass beads) and the three largest ( $\text{Al}_2\text{O}_3$ ,  $\text{SiO}_2$ , and large glass beads). Figure 7B also illustrates a fundamental property of FBRM: the tendency of the CLH to overestimate the sizes of small particles and underestimate the sizes of large particles.<sup>[29, 30]</sup> Both tungsten and the small glass beads showed a peak corresponding to a chord length that was significantly larger than its actual size range; tungsten in particular displayed this property, with the majority of the counts in its CLH distributed beyond the maximum particle size of 20  $\mu\text{m}$ . Previous research has asserted that this oversizing occurs because the beam of the laser expands beyond its focal point.<sup>[29, 30, 33, 52]</sup> If the laser contacts a particle that is smaller than the beam width, it will yield a backscattered light pulse that is closer to the width of the laser beam than it is to the width of the particle. This effect is compounded by a high number density of small particles, which increases the likelihood that the laser will encounter another particle before the previously examined particle leaves the beam.<sup>[34]</sup>

Figure 7C shows the CLH shapes from the three components with the largest radii and supports the conclusions drawn from the micrographs in Figure 6. Alumina generated fewer chord counts than silica despite having a higher number density (calculated using its average size and material density), possibly due to its smooth surface. Alumina likely generates so few counts per

particle because large portions of its surface are smooth and glassy, which would cause the FBRM laser to scatter away from the detector if it is not perpendicular to the particle surface.<sup>[59]</sup> The large glass beads, having the lowest number density of all components and the least-ideal reflection characteristics, generated the fewest counts and are difficult to detect at all – Figure 7D shows that the large glass bead histogram is consistently lower than the next smallest histogram by almost a factor of 10. All three largest components shared a peak near 3  $\mu\text{m}$ ; while their histograms above this peak appear distinctly shaped, the similarity of their CLHs may make them difficult to distinguish from each other with FBRM. Additionally, with a chord count mode less than 10, it is difficult to distinguish their signal conclusively from the noise level of the instrument. Typically, square-weighting the CLH emphasizes the chord counts generated by large particles – the square-weighted component histograms are plotted in Figure 8.



**Figure 8 – Square-weighted chord length histograms for all components. Histograms were recorded with the same material amounts as Figure 7. Note that the y-axis is not listed in units of  $\mu\text{m}^2$ , as would be expected for length-square weighting. Mettler-Toledo’s software rescales the y-axis so that the numbers are smaller and more representative of the expected counts of large particles. (A) All histograms plotted on axes that are automatically scaled for SiC. (B) The y-axis is reduced to show the shapes of the  $Al_2O_3$ ,  $SiO_2$ , and large glass bead histograms.**

Figure 8 shows that square-weighting the FBRM data emphasizes the histograms of the small particles instead of the large particles. This is because despite their large average sizes, the

largest components produce chord counts that are significantly smaller than their actual particle sizes; the inverse is true for the smallest components. Additionally, the shapes of the large component histograms become less distinct. These factors make unweighted histograms more quantitatively useful for this system.

To compute the FBRM fingerprints of the simulants components, the histograms in Figure 7 were divided by masses of material used to make each histogram. The fingerprints are plotted in Figure 9. In Figure 9B, the vertical scale is adjusted to view the histogram shapes from the three largest components.

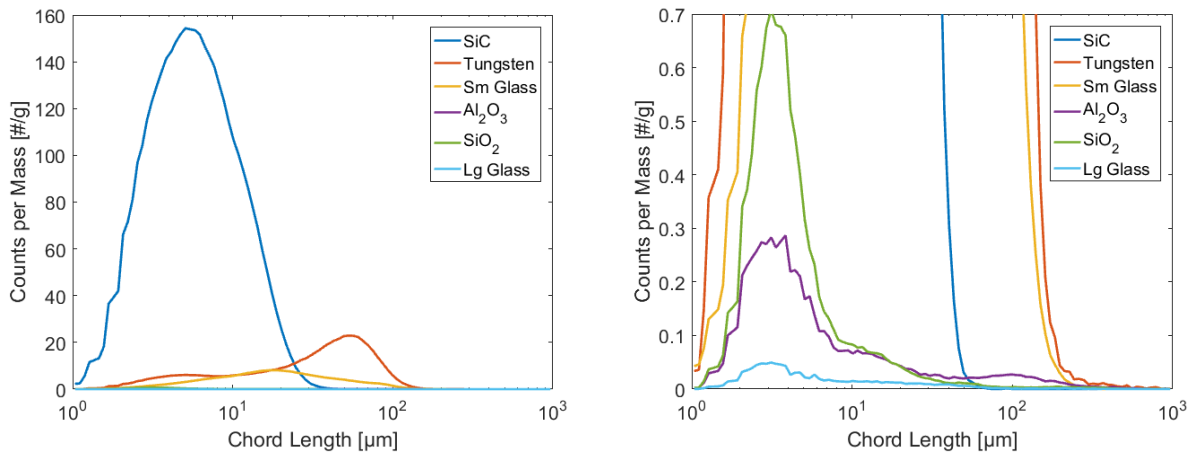


**Figure 9 – Fingerprints of the six simulants components. (A) Plots of all six fingerprints, with y-axis scaled to fit the entire SiC histogram. (B) Same curves as Figure 9A, but with the y-axis adjusted to show the scale of the three largest components.**

Figure 9 shows that SiC still generates the largest histogram in terms of counts per component mass, but its peak height is closer to the peak heights of tungsten and the small glass beads. Contrasting with Figure 7, the tungsten histogram in Figure 9 now has a higher peak than the small glass bead histogram, indicating that tungsten generates more counts on a per-mass basis. The histograms of the three components with the smallest radii still have higher peaks than the histograms of the three largest components, and the large component peak heights do not change their relative heights because all three fingerprints were recorded with the same masses (15 g of

each component). To see the difference in specific counts between the large particles, it is useful to plot the component histograms in terms of counts per particle. These normalized histograms are shown in Figure 10 (particle number was computed by assuming a spherical particle geometry, with average diameter equal to the geometric mean of the particle size range listed in Table 1).

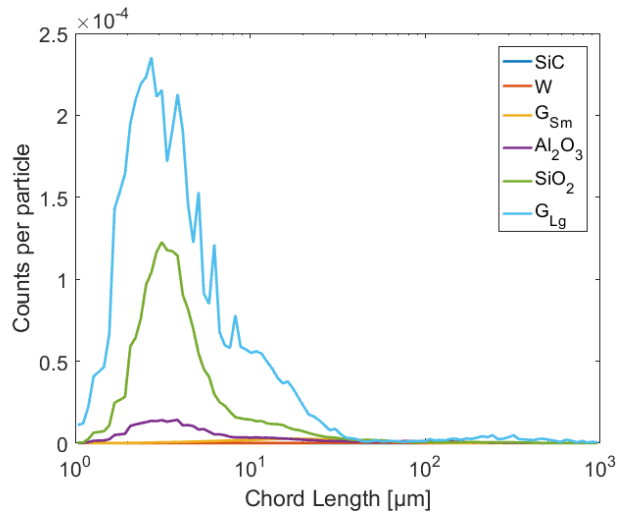


**Figure 10 – Chord length histograms of all six components, normalized by the number of particles used to record each data set.**

The CLHs in Figure 10 follow the opposite progression from those in Figure 7. Here, the large glass beads produce the most chord counts per particle by a large margin. Additionally, the difference between alumina and silica becomes more pronounced, as fewer silica particles per unit mass than there are in alumina. The three smallest components all produce significantly fewer counts per particle than the three largest components – this result is consistent with other data seen in literature, as any given large particle has a higher probability of passing in front of the FBRM laser than a small particle due to its higher cross-sectional area.<sup>[34]</sup>

Using a linear model to estimate composition with FBRM requires that the particle system being observed conform to the assumptions outlined in Section 2.3.1. For the linear model shown in Equation 2.1 to predict the composition of an arbitrary mixture of these six simulant

components, the individual fingerprints must behave linearly with respect to the total particle count. On the other hand, prior research has shown that chord count increases linearly with increasing slurry density instead of particle count.<sup>[25, 52]</sup> (Slurry density is defined as the mass of solids divided by the volume of the mixture). Figure 3, which was shown earlier to document the increase in chord count nonlinearity with increasing particle size, plotted total counts against solid fraction to illustrate this behavior. However, including the relationship between chord counts and slurry density in the PSD-CLH model would introduce nonlinearity because, as particles are added to the observed system, the total volume of the system increases. Instead of a simple  $c = Ux$  formulation, the model could take the form

$$c = \tilde{U} \left( \frac{x}{V + \rho x} \right) \quad (4.1)$$

$$\tilde{U} \in \mathbb{R}^{m \times n}$$

where  $\rho$  is the density of the solid particles,  $V$  is the liquid volume, and  $\tilde{U}$  is a modified version of the transformation matrix  $U$  that is scaled to slurry density instead of solid mass. While this relationship could be more predictive than a linear model, using it over a simple linear relationship between chord counts and particle counts is unnecessary. For every solid species, there should exist a dilute region where the simple linear relationship is valid, in which each particle contributes independently to the measured CLH. Equations 4.2 and 4.3 apply when  $x$  is small:

$$\left( \frac{x}{V + \rho x} \right) \approx \frac{x}{V} \quad (4.2)$$

$$\frac{x}{V} \propto x \quad (4.3)$$

The linear model used in this thesis can only be applied accurately in this dilute region, and finding this region for each simulant component was required before performing any composition estimation.

Testing the linearity of the CLH fingerprints of the six components was necessary prior to the model's implementation. To perform a linearity test, each component was added to pure deionized water incrementally, and the chord counts were recorded after each addition. The final amount present at the end of an experiment was greater than or equal to the amount used when the fingerprint was recorded; this way, the system's linearity could be tested for all compositions less than or equal to the maximum concentration used in the tests at NETL. The results from these experiments are shown in Figure 11, where the x-axis shows the mass of the component that has been added to 500 mL of deionized water. All histograms in Figure 11 were averaged over a period of at least 10 min to mitigate noise.

A linear regression was applied to the data for each component to find the expected chord count increase when the components are added to water – slopes alone were fit to the data, forcing the lines through the origin. Performing the regression in this way was necessary because zero counts must equate to zero observed particles. If every component's regression includes an intercept, then the model would be unable to predict an observation of zero counts. While the FBRM probe often records zero counts when monitoring pure water, there is a small amount of measurement noise. This noise was averaged over five minutes and included in the data sets shown in Figure 11. Averaging mitigated the noise as much as possible, but the average CLH of the noise was not subtracted from the background. Table 2 records the slopes of the linear regressions fitting component mass to total counts, reported in terms of total counts per gram of material, along with 95% confidence intervals on the slopes.

**Table 2 – Slopes of the linear regressions shown in Figure 11. The slope for silicon carbide is reported twice: first for the regression including all data, and second for the regression through only the region where its mass and counts appear to vary linearly (between 0 and 0.2 g). Each slope is presented with its corresponding 95% confidence interval.**

<b>Single-Component [counts/g]</b>	
SiC	5430 ± 310
SiC (linear region)	215000 ± 2000
Tungsten	573 ± 9
Small glass beads	243 ± 2
Al <sub>2</sub> O <sub>3</sub>	5.56 ± 0.15
SiO <sub>2</sub>	8.60 ± 0.31
Large glass beads	1.08 ± 0.02

Figure 11 shows chord counts plotted against the mass of each component measured separately. It can be seen that most components' behavior is at least roughly linear. Tungsten and both size ranges of glass beads show strong linearity in their fingerprints, while Al<sub>2</sub>O<sub>3</sub> and SiO<sub>2</sub> show slight nonlinear behavior. The CLHs of the three largest components were recorded with up to 15 g of material in 500 mL deionized water, which is a significantly higher concentration of these components than exists in the simulant. This high concentration was used to amplify the signal produced by the three large components; in their simulant concentrations, these components produce few chord counts and are affected more heavily by noise than the rest of the simulant. Figure 12 shows the CLH for selected solid amounts in the linearity plots from Figure 11.

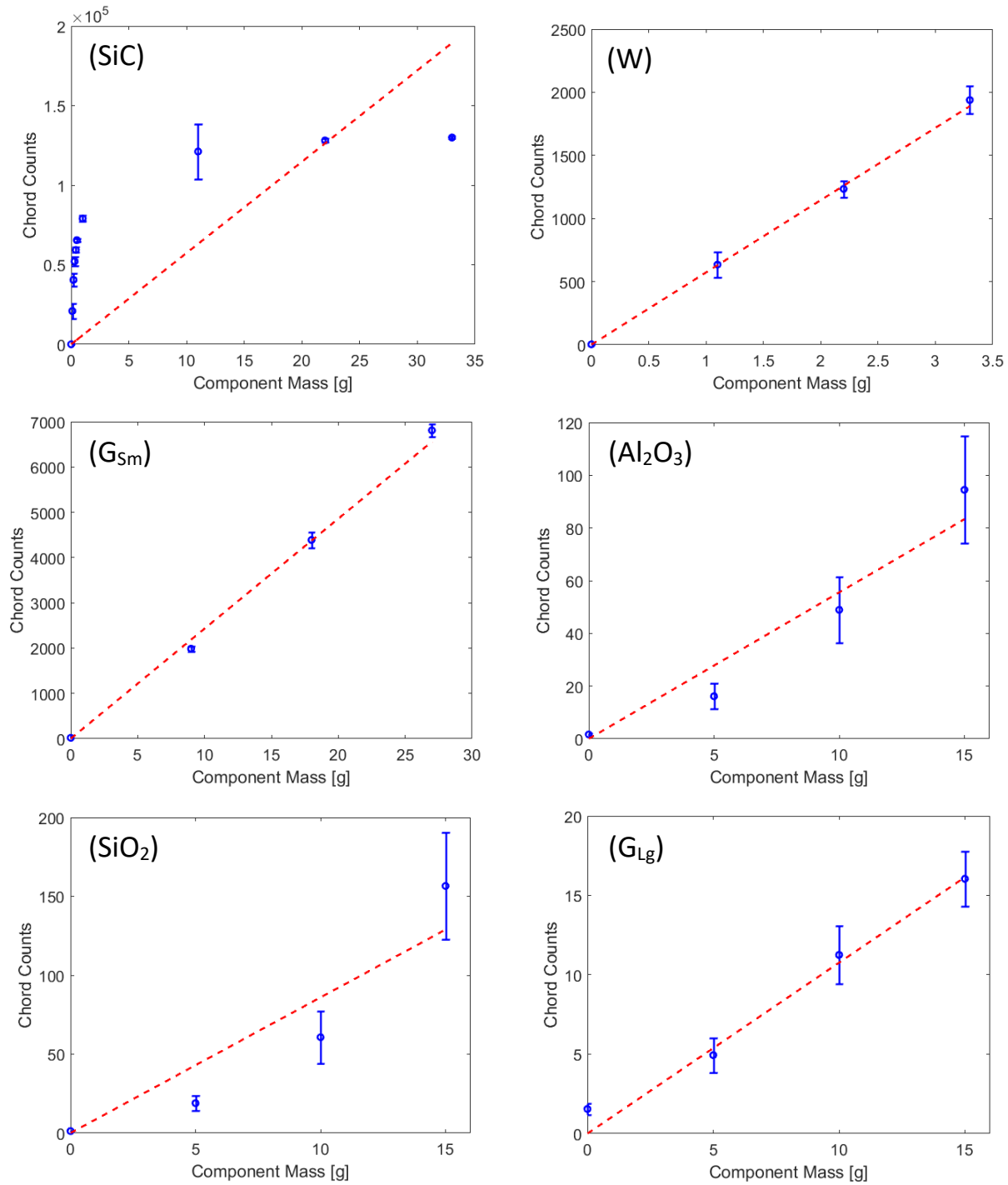


**Figure 11 – Results from linearity tests of each simulant component. The blue points are experimental data, and the dotted red line represents a linear regression to the data. All components but silicon carbide are roughly linear. Linearity is assessed in terms of solid mass. The error bars represent the standard deviation of the chord counts across the 10 minutes of averaging. They were calculated using repeated observations of the same system at intervals of 15 s, making them representative of the measurement noise.**

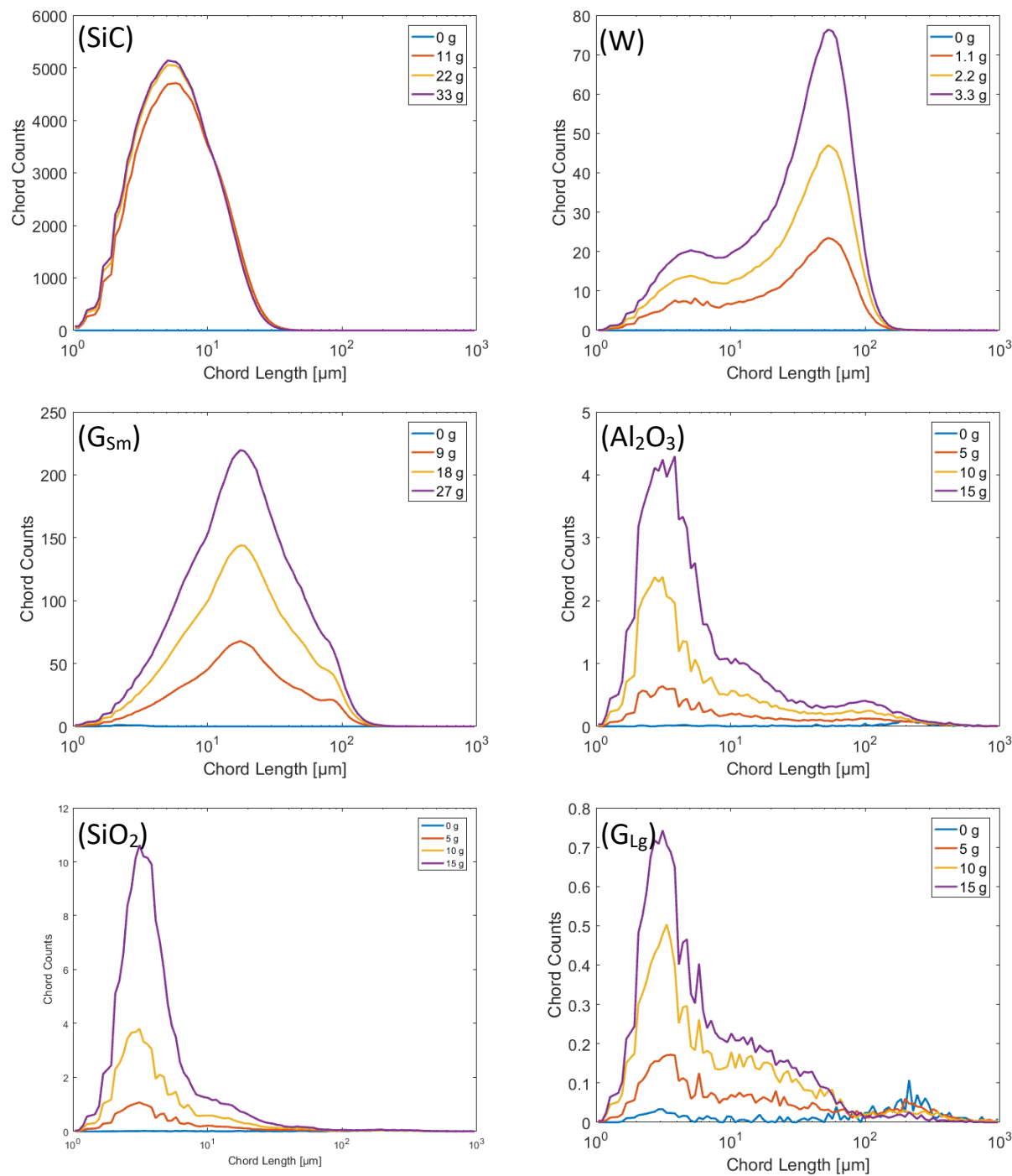


**Figure 12 – Chord length histograms from the experiments shown in Figure 9. A fixed mass of each simulant component is added to 500 mL of water at regular time intervals. Each histogram shown in this figure has been averaged over five minutes.**

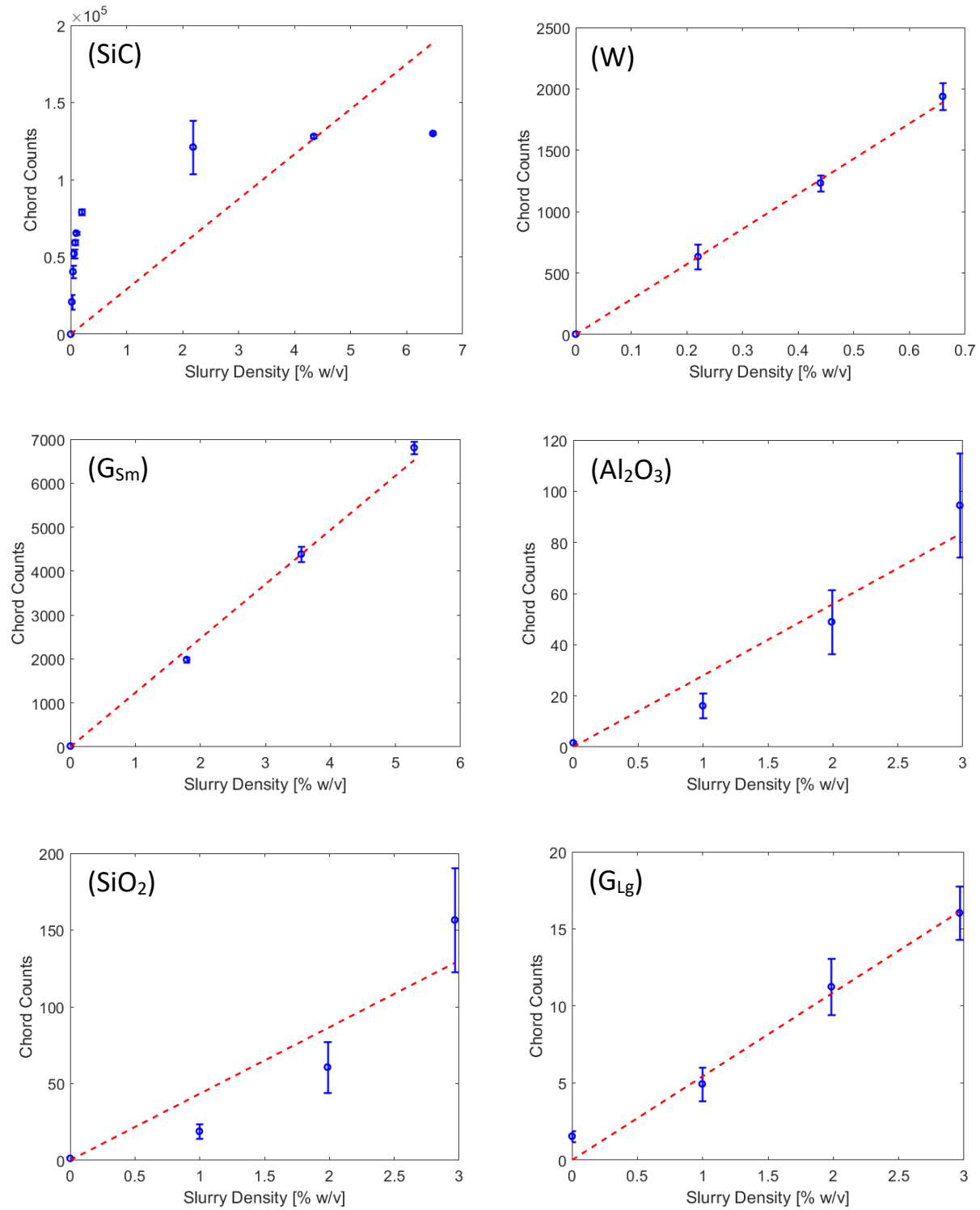


**Figure 13 – Total counts for each simulat component, plotted against slurry density to examine linearity. The blue points are experimental data, and the dotted red line represents a linear regression to the data. The error bars represent the standard deviation of the chord counts across the time interval of averaging.**

To check if the approximation denoted by Equation 4.3 is valid (that total solid mass is proportional to slurry density), the chord counts are plotted against slurry density in Figure 13. The curves in Figure 13 are similar to the curves in Figure 11. Tungsten and both size ranges of glass beads behave linearly, and some nonlinearity is observed in the plots of alumina and silica. Figure 12 shows that the shapes of the component CLHs are consistent at each addition of material, despite any nonlinearities in total chord counts. Silicon carbide is the only component that does not behave even approximately linearly, in both Figures 11 and 13.

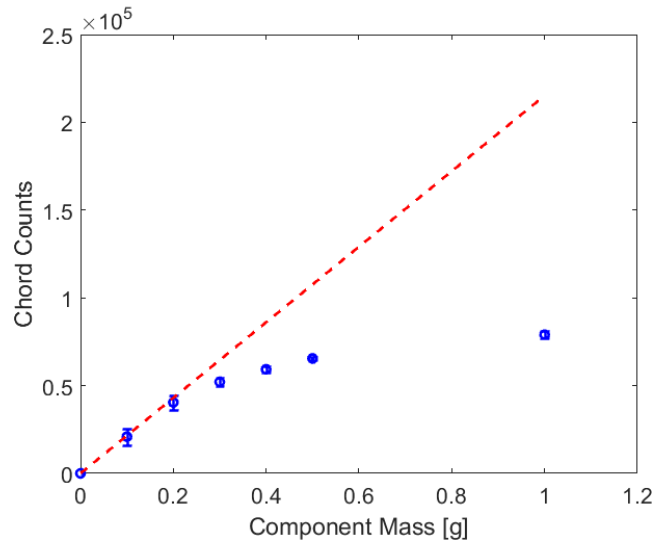
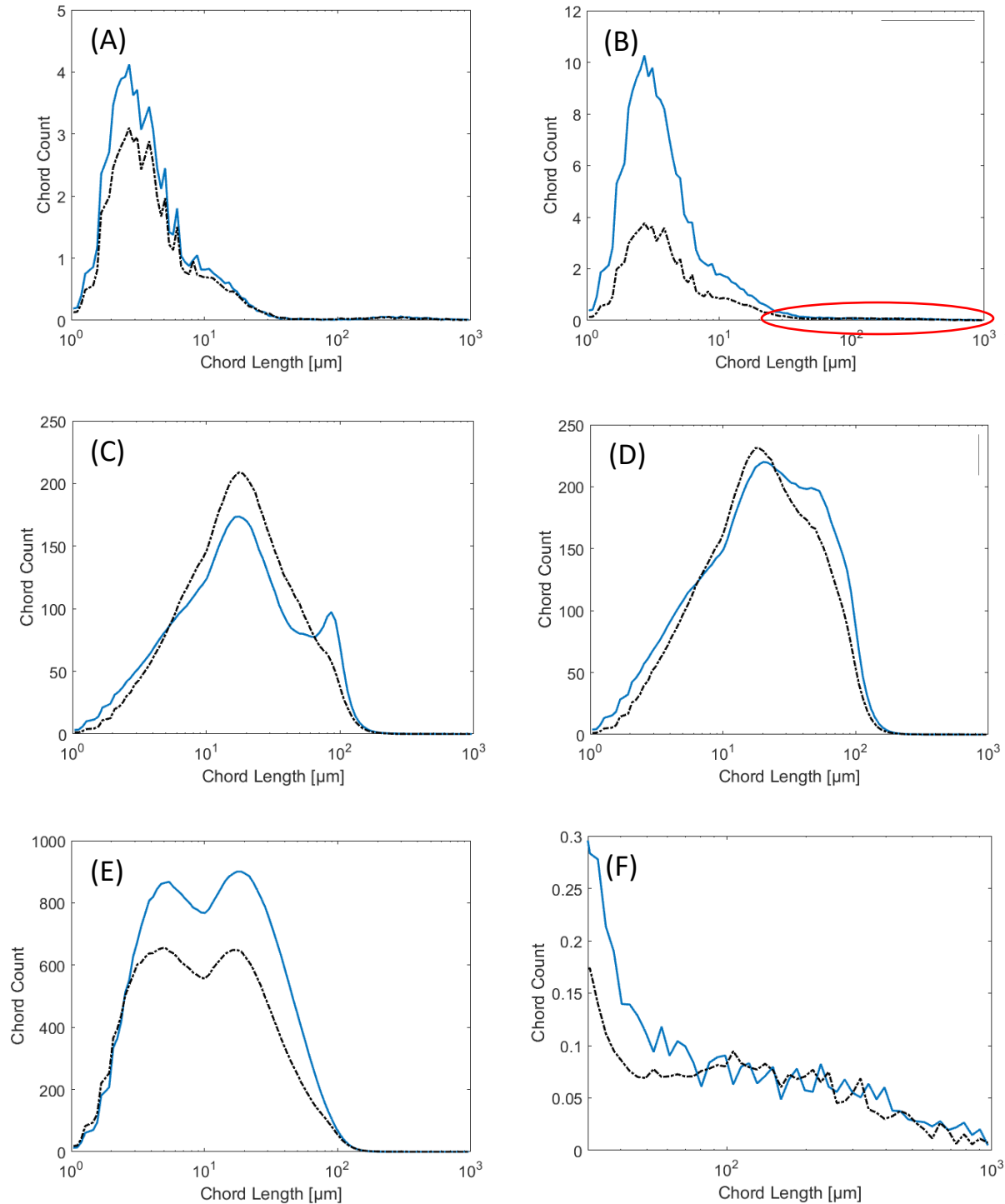


**Figure 14 – Silicon carbide total counts at small solid fractions. The blue points are experimental data, and the dashed line is a linear regression through the first three points, to show that a linear chord count region does exist. The total counts at 1 g are on the same order of magnitude as the counts at 10 g in Figure 11. The error bars are the same as those in Figure 11, where they represent the chord count standard deviations across the averaging intervals.**

Because the chord count pattern of silicon carbide looks similar to the saturation seen in Figure 2, SiC’s linearity was probed further at low masses to find a region where chords and particles varied linearly. The results of this experiment are shown in Figure 14, which once again plots total counts against the added mass of solids. This figure shows that while the linearity holds at low concentrations, the linear relationship begins to break down above 0.2 g of the component

mass, and the chord count increase from each addition of material diminishes. This behavior is not unique to silicon carbide. Comparing the trend in Figure 14 to Figure 3, which shows that sieved calcite behaves similarly to silicon carbide at higher solid fractions, the only difference between the two types of particles is the concentration at which the linear relationship breaks down.

Along with chord count linearity, the model used in this work also assumes that the component fingerprints are additive. This model assumption had to be tested for the Hanford simulant as well. To find component pairs that violated this assumption, the simulant was assembled one component at a time, starting with the largest and working down to the smallest component. The simulant was assembled according to its composition in Table 1. At each component addition, the CLH fingerprints were first multiplied by the component masses, then added together, comparing the resulting histogram to the measured CLH of the mixture to see if the fingerprints correctly reproduced its data.



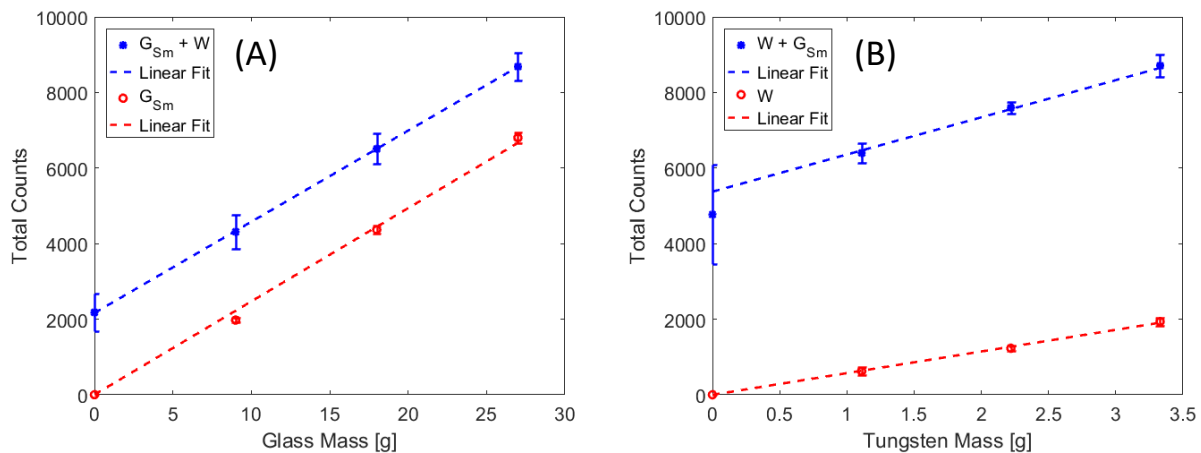
**Figure 15 – Linear combinations of the six component fingerprints, plotted alongside FBRM data taken from the component combinations mixed in 500 mL water. The solid curve is the recorded data, and the dashed curve is the model predicted CLH. (A) 0.7 g of SiO<sub>2</sub> and 1 g of large glass beads. (B) 2.4 g of Al<sub>2</sub>O<sub>3</sub> and the two components from 15A. (C) 25.6 g of small glass beads added to the components from 15B. (D) 2.7 g of Tungsten shavings and the four components from 15C. (E) 0.1 g of SiC added to the components from 15D, completing the simulant. (F) Zoom of Figure 15B to show histogram above 30 μm.**

Figure 15 shows the CLH as each component was added, starting with the mixture of SiO<sub>2</sub> and large glass beads, alongside the model's prediction of the CLH. This figure shows nonlinear behavior at each component addition via the difference between the predicted CLH and the observed data, with the most substantial changes in CLH shape occurring when the three smallest components are added. Figure 15A and Figure 15B show CLHs before and after the addition of Al<sub>2</sub>O<sub>3</sub> to the slurry of SiO<sub>2</sub>. It can be seen that the model correctly predicted the *shape* of the CLH when the largest components (Al<sub>2</sub>O<sub>3</sub>, SiO<sub>2</sub>, and large glass beads) were added; however, the magnitude of the peak at 3 μm was consistently underestimated at each step. Figure 15F plots the same data as Figure 15B, but with the axes zoomed in to show only the chords longer than 30 μm. This zoomed figure shows that, despite the higher-than-expected number of counts below 30 μm, the model correctly predicts the data for chord bins larger than 30 μm. Because the linear model shows considerably better accuracy when the counts below 30 μm are excluded, it may be desirable to exclude those counts from the model entirely; however, doing so would effectively exclude the majority of the data created by the three largest particles. The impact of these short chord counts on the components' linearity is examined more detail in Section 4.2.

Concerning the three small (SiC, tungsten, and small glass beads) components, Figures 15C through 15E all show that as they are added to the total mixture, the resultant CLH differs from the model's prediction in both shape and total counts, with the deviations from the predicted chord counts no longer being confined to purely the chord counts below 30 μm. These results necessitated examining the pairings of the small components in more detail. The additivity of component pairs was evaluated by gradually adding one component to a slurry that contained a constant amount of another component, then subsequently comparing the chord count linearity of this experiment with the linearity results of the gradually-added component in isolation. The

reverse experiment was also performed, where the component that was previously present at a constant amount was added gradually to a fixed quantity of the other component. If the slope of either component's chord count increase was unchanged while another component was present in the system, the two were considered to be additive, the ideal case.

The pairing of small glass beads and tungsten particles was found to conform partially to the assumptions of the linear model. Figure 16 compares the counts-vs-mass curves of both components in isolation and in each other's presence, showing a linear regression through both sets of points to illustrate the slope of each curve. The regressions through the component mixture data have been fit with y-intercepts to account for the initial counts generated by the first-added component, and the regressions through the pure component data are the same as those calculated from the data in Figure 11. Table 3 gives the numerical values of the two-component slopes and their corresponding 95% confidence intervals, alongside the single-component data from Table 2 for comparison.



**Figure 16 – Additivity results for small glass spheres and tungsten shavings. (A) Total counts versus mass, for glass in the presence of 3.3 g tungsten (blue curve) and in pure water (red curve). (B) Total counts versus mass, for tungsten in the presence of 27 g glass (blue curve) and in pure water (red curve). The error bars represent the chord count standard deviations across the averaging intervals.**

**Table 3 - Slopes of the linear regressions for various additivity experiments, compared to their chord count slopes in single-component mixtures. Like in Table 2, 95% confidence intervals are tabulated as well. Values for tungsten, small glass beads, and the linear region of SiC counts are colored to show comparison.**

Single-Component [counts/g]		Two-Component [counts/g]	
SiC	5430 ± 310	SiC in tungsten (linear)	205000 ± 6000
SiC (linear region)	215000 ± 2000		
Tungsten	573 ± 9	Tungsten in SiC	516 ± 28
		Tungsten in sm. glass	1190 ± 100
Small glass beads	243 ± 2	Sm. glass in tungsten	241 ± 10
Al <sub>2</sub> O <sub>3</sub>	5.56 ± 0.15		
SiO <sub>2</sub>	8.60 ± 0.31		
Large glass beads	1.08 ± 0.02		

Figure 16A shows that the pair of linear regressions have slopes that are not significantly different. This indicates that the two components, tungsten and small glass, are additive in this experiment, where the small glass beads are added to a fixed mass of tungsten. The slopes with and without the presence of tungsten are 241 and 243 counts/g, respectively. The only major difference between the two data sets is the increased noise in the two-component mixture – combining glass and tungsten creates a higher relative error at each composition, as shown by the error bars in Figure 16A.

On the other hand, the results in Figure 16A are not recreated when tungsten is added to a fixed mass of glass beads. Figure 16B, which depicts this experiment and compares it to tungsten in pure water, shows different slopes (1190 and 573 counts/g respectively) between both regressions, and the difference is large enough to be statistically significant (calculated with an F-test, using a significance value of 0.05). Despite the difference in slope, the count increase is still linear.

It is important to note that the total chord counts for 27 g of glass beads from Figure 16A are different from counts for the same sample in Figure 16B. The histograms for these two data points are plotted in Figure 17.

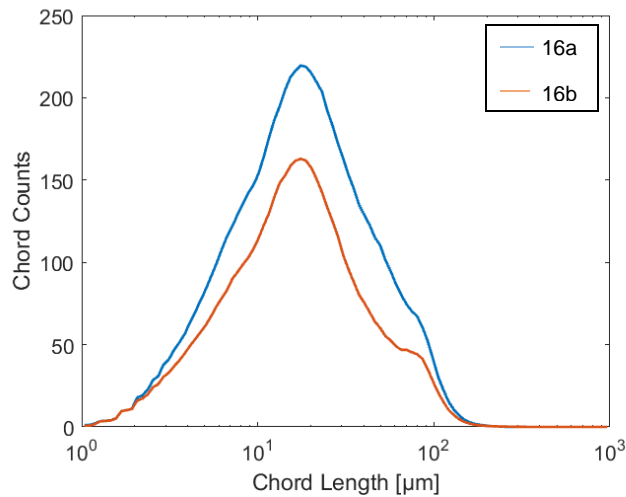


**Figure 17 – Chord length histograms recorded for samples of 27 g of small glass beads in 500 mL water, measured on two different days. Blue curve is from the measurement used for Figure 16A, red curve is from the measurement used for Figure 16B.**

The histograms in Figure 17 are offset from one another by a significant amount – their total counts differ by almost a factor of 2. Figure 17 shows the day-to-day variability that can be inherent to FBRM. This variability inhibits quantitative use of FBRM, and it sets a limit on the maximum accuracy that can be achieved for the simulant composition estimates that will be discussed in Section 4.3.

Figure 18 shows the results of the same experimental protocol in Figure 16 applied to a binary mixture of SiC and tungsten. Figure 18A compares the chord counts of SiC with and without the presence of tungsten. Due to the nonlinearity of SiC at its specified concentration in the NETL simulant, tungsten was added to the SiC slurry, where the SiC density is between 0 and 0.2 g per 500 mL of water (a number density of  $9.4 \times 10^8$  particles/L). This range is where SiC's chord count varies linearly with its particle count, as can be found in Figure 11. Like before, the numerical values of the slopes in Figure 18 are reported in Table 3.

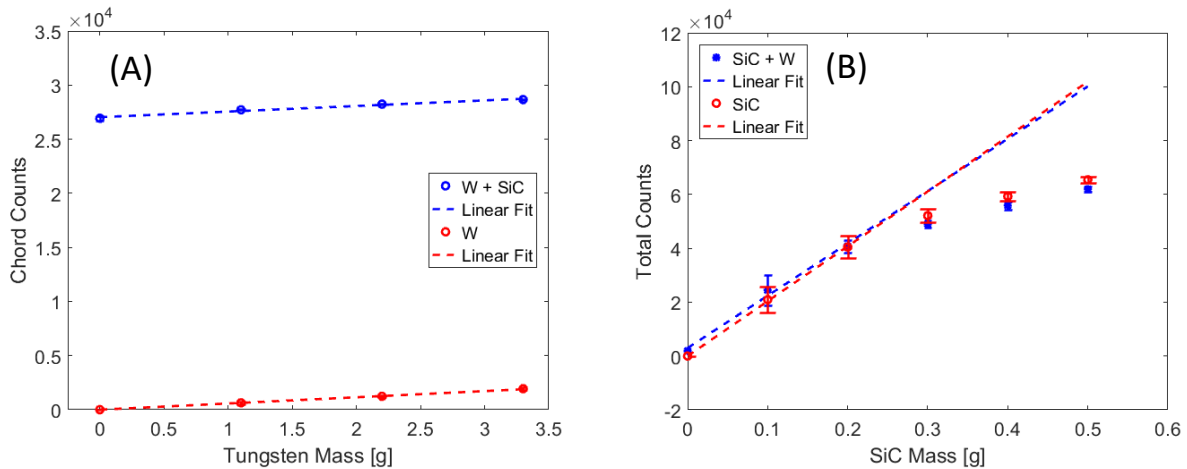


**Figure 18 – Additivity results for SiC and tungsten shavings. (A) Total counts versus mass, for tungsten in the presence of 0.1 g SiC (blue curve) and in isolation (red curve). (B) Total counts versus mass, for SiC in the presence of 3.3 g tungsten (blue curve) and in isolation (red curve) – the linear regressions are made using only data between 0 and 0.2 g of SiC.**

It can be seen in Figure 18A that the two slopes are nearly equivalent. Comparing the values in Table 3, the slope of the mixture (SiC + W) is slightly lower than the slope of pure tungsten. While these two slopes are statistically different, they differ from each other by only 10%. This observation indicates that for this component pair, the results of the additivity experiment are different the results in Figure 16 – for these two components, tungsten behaves mostly as expected when measured in the multicomponent mixture. Furthermore, when silicon carbide is added to a tungsten slurry (Fig. 18B), it produces a visibly similar chord count increase to pure silicon carbide – these two slopes are not statistically different with a significance value of 0.05.

## 4.2 Chord Length Error Analysis

Previous work by Li et al.<sup>[31, 64, 65]</sup> excluded counts from size bins smaller than  $30 \mu\text{m}$  due to high noise and a less robust dependence on the actual number of particles. To evaluate the noisiness of counts below  $30 \mu\text{m}$  for the waste simulant used in this work, the standard deviation of the total chord counts was calculated for each component. Each standard deviation was calculated using 10 minutes of recorded CLHs, yielding 40 total measurements for each

component. The standard deviations were divided by the average chord counts to represent the relative error. The results of these calculations are shown in Table 4, which shows this relative standard deviation for chords both above and below 30  $\mu\text{m}$ .

**Table 4 – Standard deviation of total counts measurement, as a percent of the total counts. Deviations were calculated for chord counts both below and above 30  $\mu\text{m}$ .**

	SiC	W	Sm Glass	Al <sub>2</sub> O <sub>3</sub>	SiO <sub>2</sub>	Lg Glass
<b>1-30 <math>\mu\text{m}</math></b>	7.84%	9.02%	2.68%	29.5%	25.8%	21.2%
<b>30-1000 <math>\mu\text{m}</math></b>	7.69%	8.84%	2.54%	15.8%	15.0%	21.9%

In Table 4, it is immediately apparent that two components, Al<sub>2</sub>O<sub>3</sub> and SiO<sub>2</sub>, see a significant reduction in relative error for chords longer than 30  $\mu\text{m}$ , while the other components see little to no change with these chords removed. These two components are similar in size and share a similar surface character, so it is not surprising that they should behave similarly to each other under FBRM monitoring. However, this reduced error was not seen for the other type of large particle, the 841-1190  $\mu\text{m}$  glass beads. All three of these components have a large CLH peak centered at 3  $\mu\text{m}$ , which was seen previously in Figure 7. This peak is thought to exist because of chord splitting, a phenomena discussed in the background section where interruptions in the backscattering along a large particle cause it to generate multiple short chords instead of a single long chord. The results in Table 4 indicate that the glass beads likely experience chord splitting in a more consistent manner than Al<sub>2</sub>O<sub>3</sub> and SiO<sub>2</sub>, as glass beads do not feature significantly different levels of error between the chord splitting peak and the rest of the histogram. When a transparent glass bead is scanned by the probe's laser, it will produce bright spots that are uniform regardless of its rotation, and any one particle backscatters light in a similar pattern to its neighbors due to the spherical shape of glass beads in a population. Al<sub>2</sub>O<sub>3</sub> and SiO<sub>2</sub>, by contrast, are not uniformly shaped and may present distinct faces to the probe when rotated. While the effect of rotation would

be expected to average out over a large number of particles, the number of sampled particles is very small in the waste simulant.

Having determined that excluding chords shorter than 30  $\mu\text{m}$  reduces noise for  $\text{Al}_2\text{O}_3$  and  $\text{SiO}_2$ , it was next necessary to test whether or not those chords behaved more nonlinearly than the larger chords. This was tested with the data sets used in Figure 8, which consisted of CLHs measured at different concentrations of each component. By isolating the total chord counts above and below 30  $\mu\text{m}$ , then applying a linear regression to each set of chord counts, it was possible to calculate the goodness of fit for each set of chords. The  $R^2$  values from each regression are presented in Table 5.

**Table 5 –  $R^2$  coefficients for the linear regression between chord counts and solid mass. These coefficients were calculated for counts above and below 30  $\mu\text{m}$ ; SiC considered only the linear region at small mass fractions shown in Figure 7.**

	SiC	W	Sm Glass	$\text{Al}_2\text{O}_3$	$\text{SiO}_2$	Lg Glass
<b>1-30 <math>\mu\text{m}</math></b>	0.996	0.981	0.992	0.758	0.712	0.893
<b>30-1000 <math>\mu\text{m}</math></b>	0.999	0.979	0.985	0.906	0.801	-0.392
<b>1-1000 <math>\mu\text{m}</math></b>	0.997	0.965	0.981	0.789	0.717	0.900

Table 5 shows similar results to Table 4, in that most components showed no significant difference in linearity between chords above and below 30  $\mu\text{m}$ , and that  $\text{Al}_2\text{O}_3$  and  $\text{SiO}_2$  were the only components to show improvement with the short chords removed. However, the large glass beads behaved less linearly with the short chords removed, an unexpected result given the minimal difference in standard deviation between long and short chords for this component. This nonlinear behavior likely occurs because the bulk of this component's CLH is smaller than 30  $\mu\text{m}$  – because the large glass spheres are smooth and transparent, it is highly unlikely that the FBRM laser is able to measure their full diameter. Because all spherical beads cause chord splitting in a similar manner, the chord counts below 30  $\mu\text{m}$  still vary linearly with the particle count.

Tables 4 and 5 show that for  $\text{Al}_2\text{O}_3$  and  $\text{SiO}_2$ , there could be an increase in model accuracy if the counts below  $30\ \mu\text{m}$  are excluded from the fit – the long chords show a smaller standard deviation and a greater  $R^2$  value than the short chords for both components. All other components show little to no improvement between these chord sizes, and slurries including the large glass beads will see an accuracy decrease. Because two large components could be positively affected, and the large glass beads are difficult to detect in the presence of any other components to begin with, it may be beneficial to exclude these counts from the model when measuring most component combinations. However, excluding these counts from the fit would remove almost half of the bins in the CLH, so versions of the model with and without these bins were tested on real data and compared.

### **4.3 Model Accuracy**

Testing the model assumptions provided necessary context for application of the model to real data. The model was used to estimate the composition of component pairs and mixtures before applying it to data from the full simulant. This section documents the model's estimates when applied to these data sets.

We use the same data shown in Figure 16 to test the model, where tungsten and small glass beads were mixed together in 500 mL of deionized water. At every tested composition, data was recorded over a period of time so that when averaged, it would provide a consistent measurement. For this system, the CLH was averaged over a period of 5 minutes. This shorter averaging time was possible for this system due to the high total chord counts — systems with lower total counts necessitate longer observation periods to reduce the noise level.

Figure 19 shows the results from the model's application to data, recorded according to the procedure outlined above, from a mixture of 3.3 g of tungsten and 27 g of small glass beads in suspension. Figures 19A, 19C, and 19E respectively plot the unmodified linear empirical model's estimate, the model's estimate using the AIC-based component selection step, and the model's estimate both using the component selection step and excluding chord counts smaller than 30  $\mu\text{m}$ . Each estimate is shown alongside a plot containing three CLHs, which represent in order: the CLH measured from the mixture of 3.3 g of tungsten and 27 g of small glass beads, the linear fit of the dataset using the component fingerprints, and the model's prediction of what the CLH should look like (created by linearly combining the component fingerprints, weighted by the component amounts).

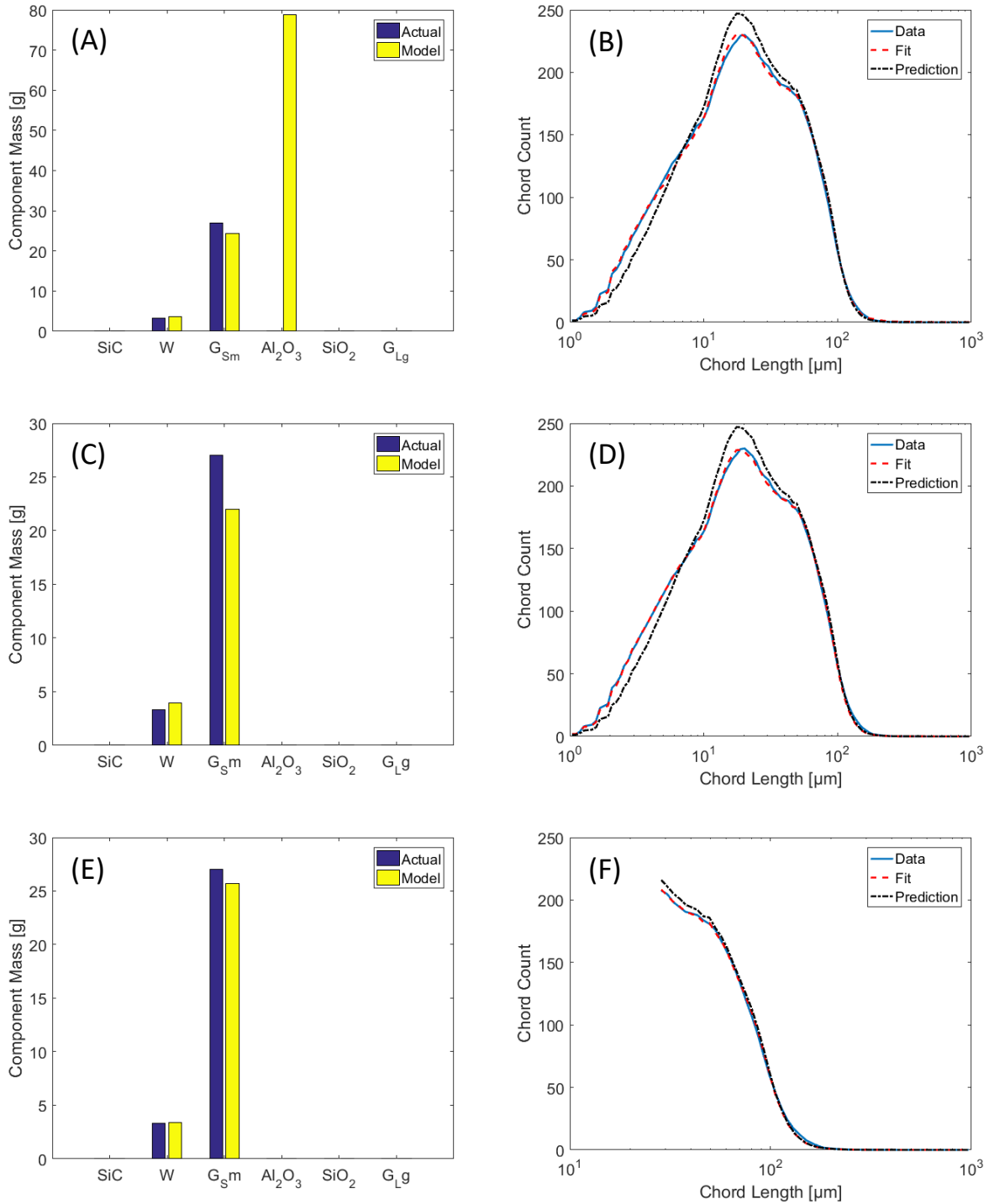


**Figure 19 – Composition estimates from the model for a mixture of 3.3 g tungsten and 27 g of small glass beads. (A) Composition estimate made by the unmodified linear model. The blue bars indicate the slurry’s true composition, and the yellow bars indicate the model’s estimate. (B) Plot of the actual measured CLH, the best-fit CLH using the linear model, and the linear model’s prediction of what the ideal CLH should look like. (C) Composition estimate using the AIC component selection step. (D) CLH plot for 19C. (E) Composition estimate using the AIC component selection step and excluding counts below 30 μm. (F) CLH plot for 19E.**

Figure 19E shows the most accurate estimate, in which the component masses are accurate to within 10% of their actual values. The model used to make the estimates in Figure 19E incorporated the component selection step and excluded counts below 30  $\mu\text{m}$ .

Comparing Figures 19A and 19C shows that without the component selection step described in Section 3.5, the model estimates 80 g of alumina that is not present in the mixture, while the two components that are actually present remain mostly unchanged by this model modification. Using the lowest AIC to select the optimal number of components was adequate to properly balance goodness of fit with model simplicity, for the two-component system used in Figure 19. The red dashed curves in Figures 19B and 19D, which represent the model's least-squares fit of the data, are almost identical; this similarity shows that the addition of alumina is insensitive to the CLH.

Excluding the short counts visibly improved the estimation accuracy. Both Figures 19C and 19E show that the lowest AIC model selects the correct two components regardless of the count exclusion, but the quantities of both are closer to their actual values with these counts excluded. This is a surprising result, as the analysis in the previous section showed that excluding the small counts does not lower the count variance for the two small components considered here. Here, Figures 19C and 19E show that excluding counts shorter than 30  $\mu\text{m}$  positively affects this two-component system. Despite this result, there is also significant information content lost, comparing the CLH in Figures 19D and 19F.

As mentioned previously, the model can operate on noisy data sets collected in real time and return composition estimates accurate to within FBRM's inherent level of error. Figure 20 shows the model's estimates at each time point along an entire experiment. The estimated composition corresponded closely to the actual experimental procedure. First 3.3 g of tungsten was

added to pure water, the same amount examined in Figures 16 and 18. The CLD was measured for 5 minutes, at which point 9 g of glass spheres were added to the mixture. This addition was repeated two more times, at 5 minute increments.

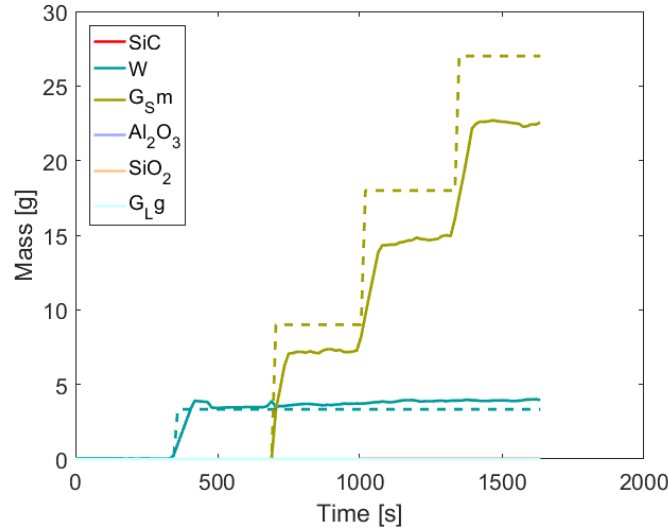


**Figure 20 – Real-time composition estimate for the experiment performed in Figure 16A and Figure 19. The solid lines indicate the model-predicted composition, and the dashed lines represent the actual composition. The AIC component-selection step is used in this model, and the model considers all chord counts between 1 and 1000  $\mu\text{m}$ .**

The model accurately estimated the tungsten concentration throughout the entire experiment, and while it underestimated the amount of glass added at each step, it registered equal additions of the components at the appropriate times, suggesting linearity. There was a small time lag for the composition estimate to reach a steady state after each addition, owing to the time it takes for the slurry to become completely mixed. Once this steady state was reached, the estimate remained steady until more material was added to the system.

The estimation accuracy attained in Figure 20 does not hold for all mixtures. Considering the potentially nonadditive behavior of small glass beads and tungsten shavings illustrated by Figure 16 and Table 3, the composition of the slurry in Figure 20 can still be tracked approximately. The amounts of each component are underestimated at each step because mixing

these components together does not always produce the same chord count increase as the components do individually. However, applying the model to the experimental profile from Figure 16B, which uses the same two components, does not yield the same level of success.

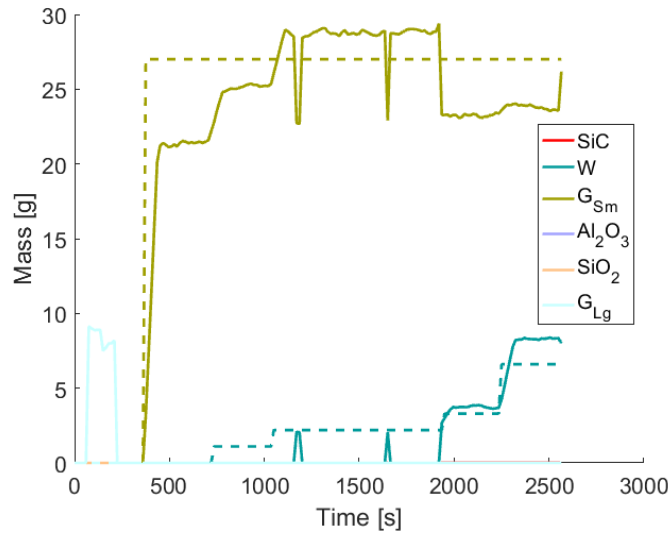


**Figure 21 - Real-time composition estimate for the experiment performed in Figure 16B. The solid lines indicate the model-predicted composition, and the dashed lines represent the actual composition. The AIC component-selection step is used in this model, and the model considers all chord counts between 1 and 1000  $\mu\text{m}$ .**

Figure 21 shows a real-time composition estimate for the experiment performed in Figure 16B, where a fixed mass of glass beads was added initially, followed by successive additions of tungsten. In this case, the model was incapable of distinguishing the tungsten additions from more glass beads. Only at 2000 seconds, when the third mass of tungsten was added to the mixture, did the model converge to an estimate more representative of the actual composition.

While the two-component mixture of small glass spheres and tungsten shavings allowed for composition estimation using the linear model, the mixture of silicon carbide and tungsten could not be estimated with the same level of accuracy. Figure 22 shows the model's best composition estimate for a mixture of these two components.

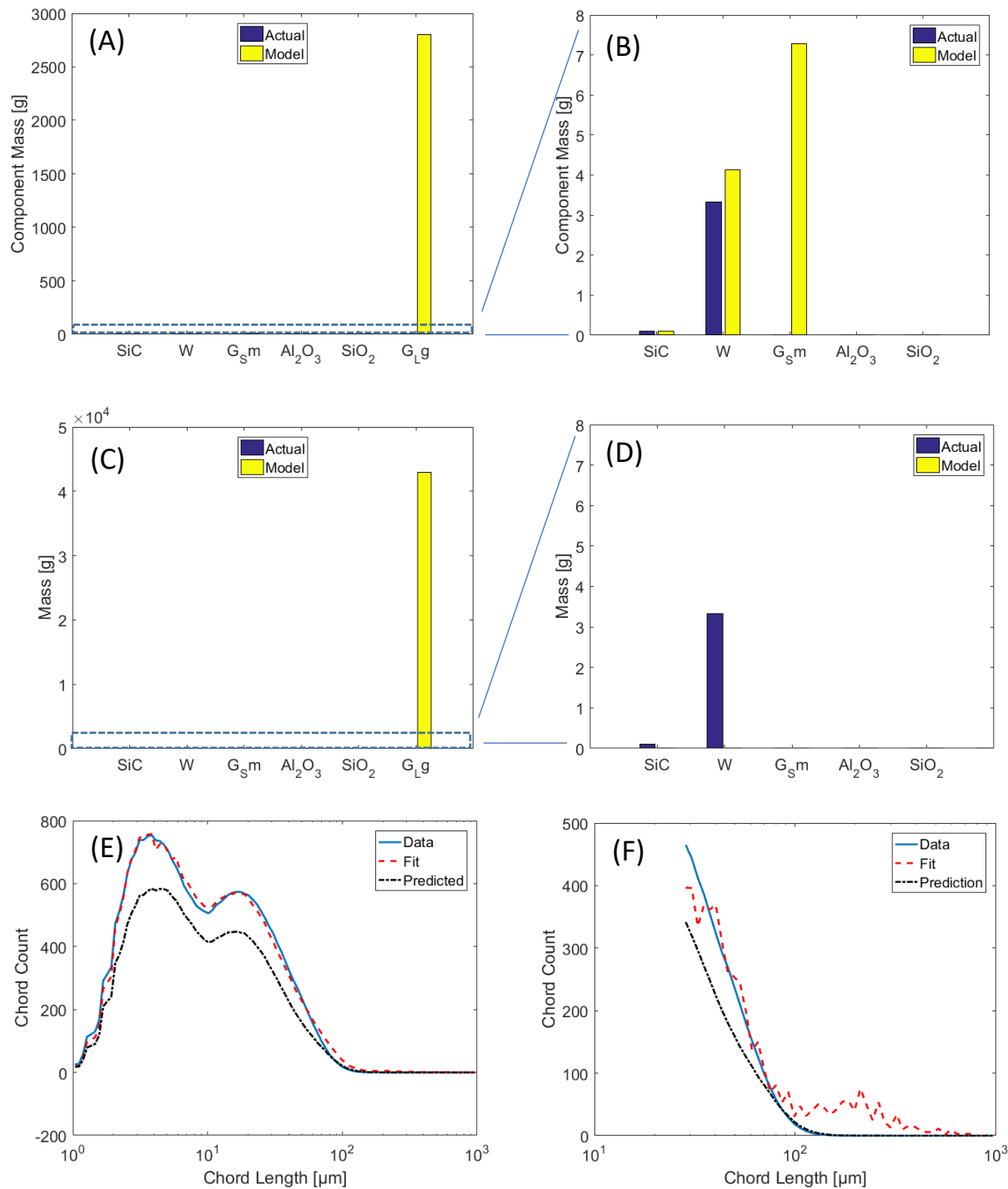


**Figure 22 – Composition estimates for a mixture of 0.1 g SiC and 3.3 g tungsten shavings. (A) Composition estimate using the AIC component selection step. (B) Same data as Figure 22A, but with the y-axis zoomed to show mass estimates other than large glass beads. (C) Composition estimate using the AIC component selection step, excluding counts shorter than 30  $\mu\text{m}$ . (D) Same data as Figure 22C, with the y-axis zoomed to show mass estimates other than large glass beads. (E) CLH plot for Figure 22A. (F) CLH plot for Figure 22C.**

The AIC is employed to calculate the optimal number of components in all estimates, and results are shown both including and excluding counts shorter than 30  $\mu\text{m}$ . CLH plots of the type used in Figure 19 are also shown.

The actual amount of material present upon recording this data set was 0.1 g of SiC and 3.3 g of tungsten. The model did correctly recognize the presence of these two components, but it added substantial amounts of both sizes of glass beads to its estimate. The large glass beads in particular were predicted to be present at a mass that is orders of magnitude greater than any other component, both including and excluding the short chord counts. Additionally, Figures 22B and 22C show that both quantities of the components that were actually present were overestimated by about 20%.

The linear model's failure to capture the behavior of this system was unexpected, given the additivity of silicon carbide and tungsten at low SiC concentrations. Figures 22E and 22F show a distinct difference between the model's predicted CLH and the actual data. In order to compensate for this difference, the model added excess amounts of both SiC and tungsten. The model also added the fingerprint from the large glass beads to the fit, which explains the noisiness of the dashed red curves in both CLH plots (Figures 22E and F). Due to the large glass beads producing few counts per gram of material, they were estimated in high numbers even though they contributed relatively few total counts to the fit. Figure 22F shows that when the short counts were excluded, the data set did not contain enough detail to allow for a unique solution, so the model was unable to estimate the present amounts of either SiC or tungsten.

In summary, the model's applicability to the three small components in the simulant was mixed – it predicted combinations of tungsten and glass beads with moderate accuracy, but mixtures including SiC were difficult to analyze with a linear model. The three large components

(alumina, silica, and large glass beads) produced fewer total counts than the small components, so they were examined separately before examining the simulant that contains six components.

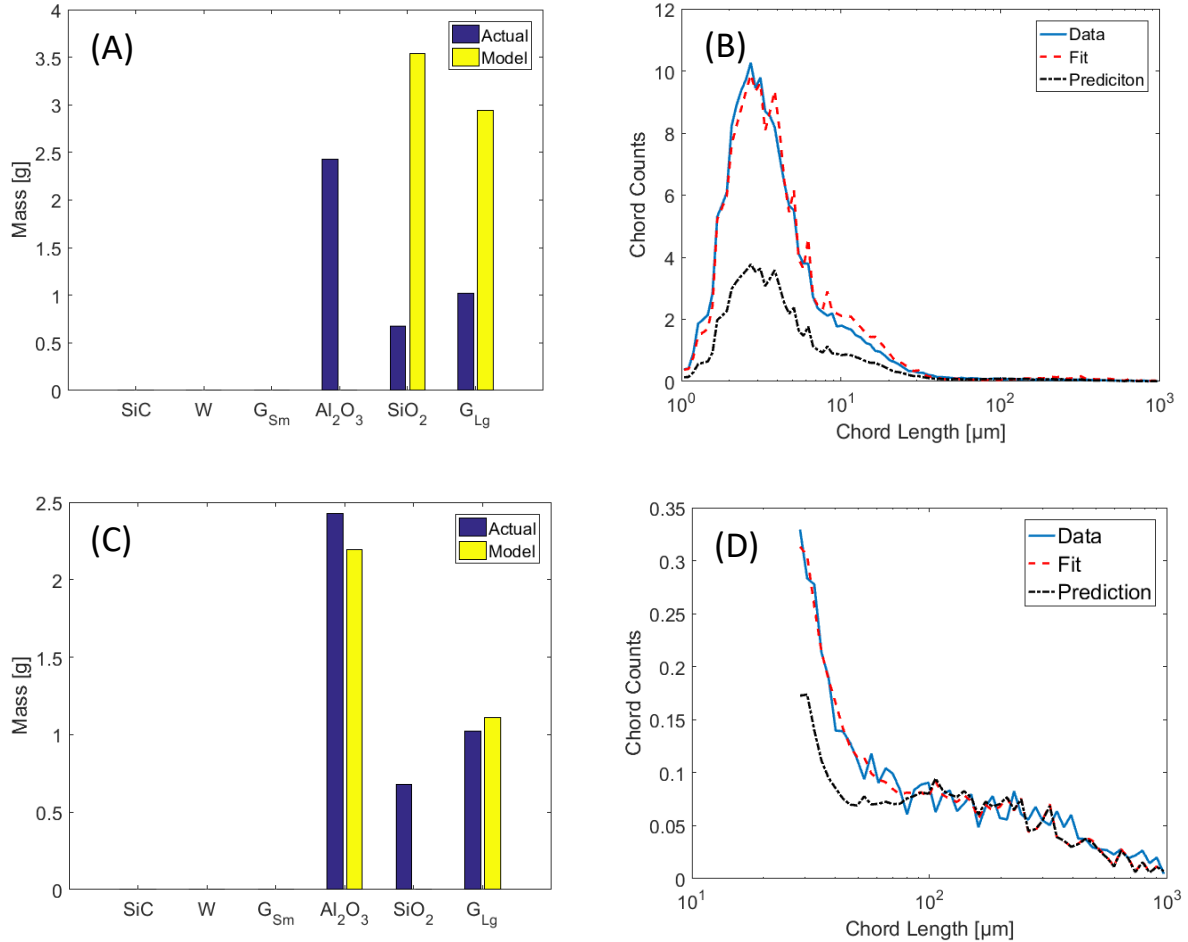


**Figure 23 – Composition estimates for slurry containing 2.4 g alumina, 0.7 g silica, and 1 g of large glass beads. (A) Model estimate compared to actual composition, using the full range of chord lengths. (B) CLH plot showing the FBRM data for the mixture, the model's best-fit CLH, and the model's prediction of what the CLH should be. (C) Model estimate of composition, using only counts longer than 30 μm. (D) Same curves as Figure 23B, but using counts longer than 30 μm.**

Figure 23 shows the model's best concentration estimates for a slurry of 2.4 g of alumina, 0.7 g of silica, and 1 g of large glass beads. Composition estimates both including (Figure 23A and B) and excluding (Figure 23C and D) counts below 30 μm are compared. Figure 23A compares the model estimate and actual composition, which illustrates a significant overestimation of both silica and the large glass spheres, while the 2.4 g of alumina in the slurry is not seen at all. Figure

23B compares the CLH and the fitted model. The three CLHs plotted in this figure show that this overestimation occurs due to a difference in the peak magnitude at 3  $\mu\text{m}$ . The model predicted that this peak should be substantially lower, and thus it increased the concentrations of the components whose fingerprints most prominently feature that peak.

In Figure 23C, the same comparison of the model estimate and actual composition is shown, where chord counts smaller than 30  $\mu\text{m}$  are eliminated. As shown earlier, chord counts shorter than 30  $\mu\text{m}$  are more variant than counts larger than 30  $\mu\text{m}$  for both alumina and silica. A reduction is seen in concentrations that were previously overestimated. However, excluding the small counts changed the component that has been left out of the estimation – previously, alumina was not detected by the model, and with the modified model, silica shows an estimated concentration of zero.

Figure 23D shows plots for the fitted and measured CLDs. It can be seen that despite the absence of silica, the predicted CLH and the observed data match closely, while the only major difference is found between 30 and 100  $\mu\text{m}$ . This means that silica likely generates the majority of its counts below 30  $\mu\text{m}$  – the silica histogram in Figure 8 supports this conclusion. If silica does generate a substantial number of counts above 30  $\mu\text{m}$ , then the model's predicted CLH would deviate further from the observed data than it does in Figure 23D. Additionally, because Table 4 has already demonstrated that the counts above 30  $\mu\text{m}$  generated by the large glass beads do not behave linearly, it is reasonable to conclude that the improved accuracy of the large glass beads' mass estimate is due to luck. The majority of the observed counts in that region are likely generated by alumina alone, which helps to explain why the estimated mass of alumina is so accurate.

When the entire simulant was tested with FBRM, the three smallest components generated so many chord counts that the three largest components were nearly indistinguishable from

background. Figure 24 shows the linear model's best estimate of the full simulant composition. The data collected to make this figure was taken from a slurry containing all components in the concentrations specified in Table 1, with one exception: silicon carbide was added at a concentration that was within the linear region of Figure 14 (below 0.2 g of SiC). Limiting the amount of SiC was necessary because it completely masked the signals from the other components if used at its concentration specified in Table 1.

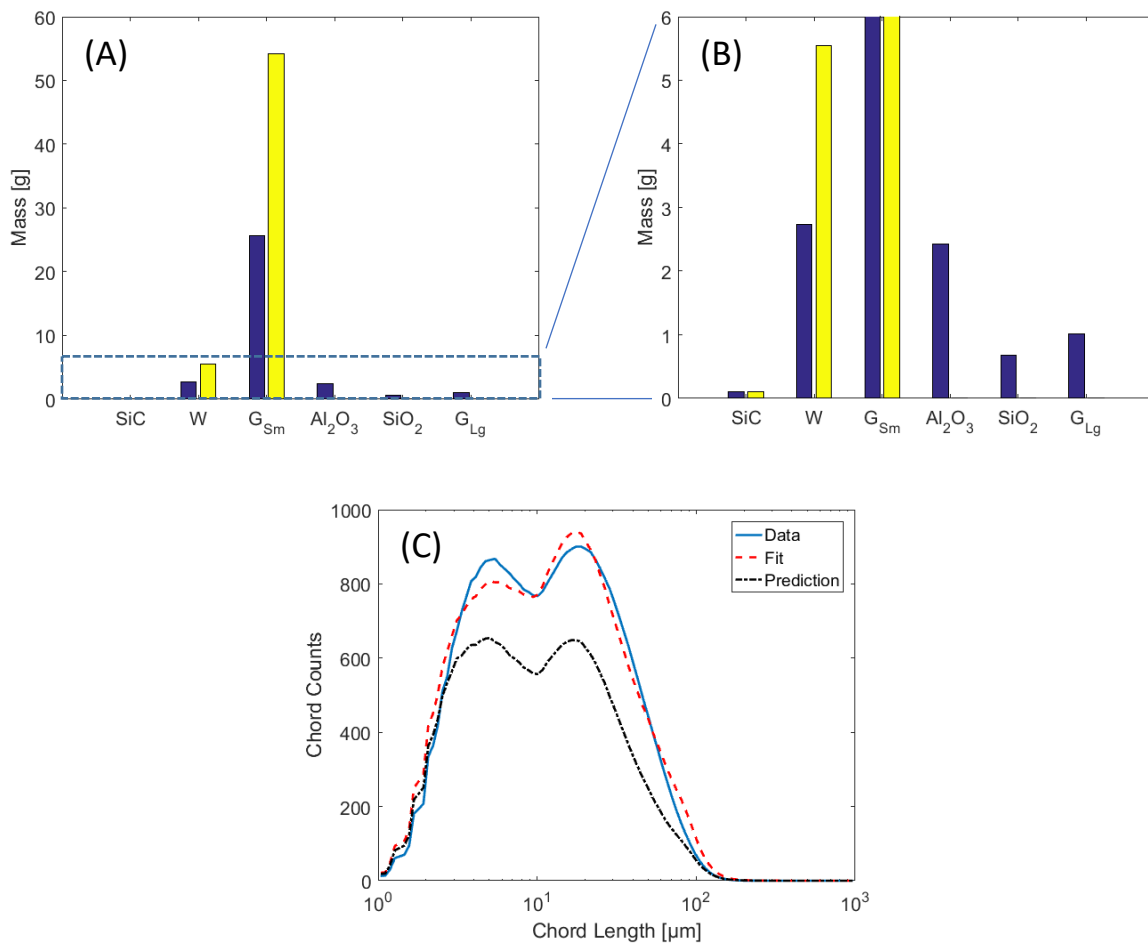


**Figure 24 – Composition estimate for the full simulant containing 0.1 g SiC, 2.7 g tungsten, 26 g small glass beads, 2.4 g alumina, 0.7 g silica, and 1 g large glass beads. Silicon carbide is present in this small concentration so that its chord counts remain linear. The model operated on the full range of chord length bins, from 1 to 1000 μm. (A) Model estimate compared to actual composition. (B) Zoom of (A) to show that SiC is correctly estimated, and all three large components are absent. (C) CLH plot showing the model prediction and fit.**

Figures 24A and 24B show that the model is unable to estimate the concentrations of the large components in this mixture. These components generated so few chord counts that they were indistinguishable among the more numerous particles of the small components. Alongside this error, the model overestimated the concentrations of both tungsten and the small glass beads, while its silicon carbide estimate remained accurate. Figure 24C, which compares the measured FBRM data to the model's predicted CLH and the best-fit CLH calculated by regression, shows why this overestimation occurs. In this system, the linear model underestimated the total counts that the particles actually produced, which caused it to overestimate the component concentrations to make up the difference.

For this system, removing the counts below 30  $\mu\text{m}$  from the model did not allow the model to see the large components, nor did it improve the estimation accuracy of the small components. Figure 25 shows the composition estimate for the full simulant, using only counts above 30  $\mu\text{m}$  in the fit. The composition is shown in Figure 25A alongside the CLH plot in Figure 25B.

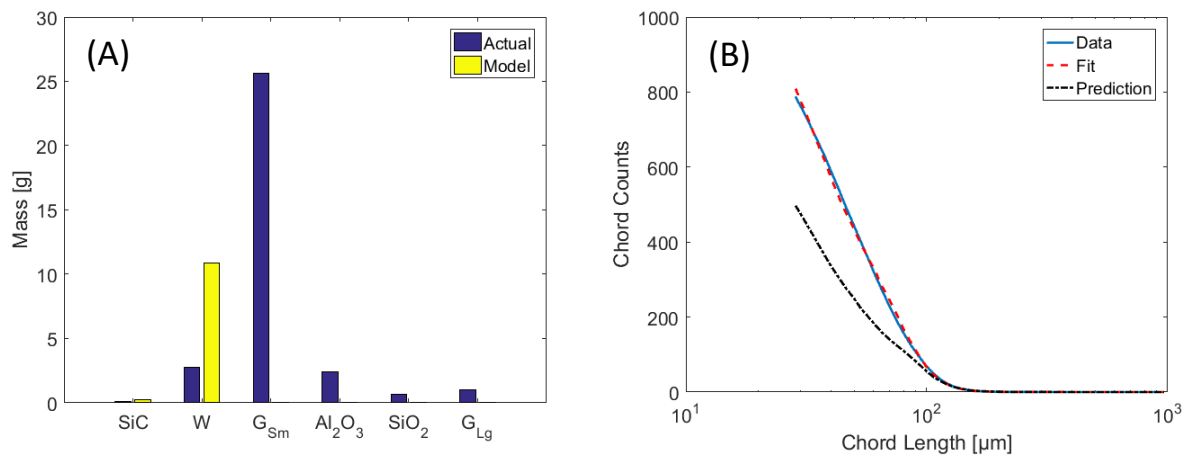


**Figure 25 – Composition estimate for the full simulant containing 0.1 g SiC, 2.7 g tungsten, 26 g small glass beads, 2.4 g alumina, 0.7 g silica, and 1 g large glass beads. The model operated only on chord length bins between 30 and 1000  $\mu\text{m}$  to produce this estimate. (A) Model estimate compared to actual composition. Alumina, silica, and both glass bead sizes show zero mass. (B) CLH plot using the whole simulant and excluding counts below 30  $\mu\text{m}$ .**

Removing the small counts from the model resulted in a less-accurate composition prediction. SiC and tungsten were overestimated to a greater degree, and the model failed to detect any of the other components. Figure 25B shows that the difference between the model-predicted CLH and the real data remains present – with this model, silicon carbide and tungsten together are able to perfectly recreate the data set without the excluded counts. Due to the simple shape of the histogram above 30  $\mu\text{m}$ , excluding the small counts from the model is not feasible when all three small components are present.

#### **4.4 Model Modifications**

An option for improving the results for mixtures with silicon carbide is adding the length-square weighted CLH to the model fit. Mettler-Toledo's iC FBRM software is capable of automatically weighting the CLH by the square chord length in each bin. According to Mettler-Toledo, the unweighted CLH is typically most sensitive to particles with high number densities. Square-weighting the CLH emphasizes the longer chord counts and makes the CLH more sensitive to particles that make up a large volume fraction of the monitored slurry. While silicon carbide's average size is the smallest of any of the components, it does generate some of the longest chord counts of any components, which should allow its concentration to be better represented by a square-weighted CLH.

Adding square-weighted data to the model requires modifying the least-squares objective function. Unweighted and square-weighted histograms have different total chord count numbers, which biases the total sum-squared error towards the unweighted fit. To account for this, both SSEs were scaled in the objective function

$$\min_x \frac{c_{sq}}{c} \sum_{j=1}^m (u_j x - b_j)^2 + \frac{c}{c_{sq}} \sum_{j=1}^m (u_j^{sq} x - b_j^{sq})^2 \quad (4.4)$$

where  $c$  and  $c_{sq}$  are the unweighted and square-weighted total counts, from vectors  $b$  and  $b_{sq}$  respectively,  $u_j$  and  $u_j^{sq}$  are the rows of the unweighted and square-weighted fingerprint matrices, and  $m$  is the number of bins in the CLH. This modified objective function combines the sum-squared errors of the unweighted and the square-weighted CLHs in a way that ignores any difference in total chord counts.

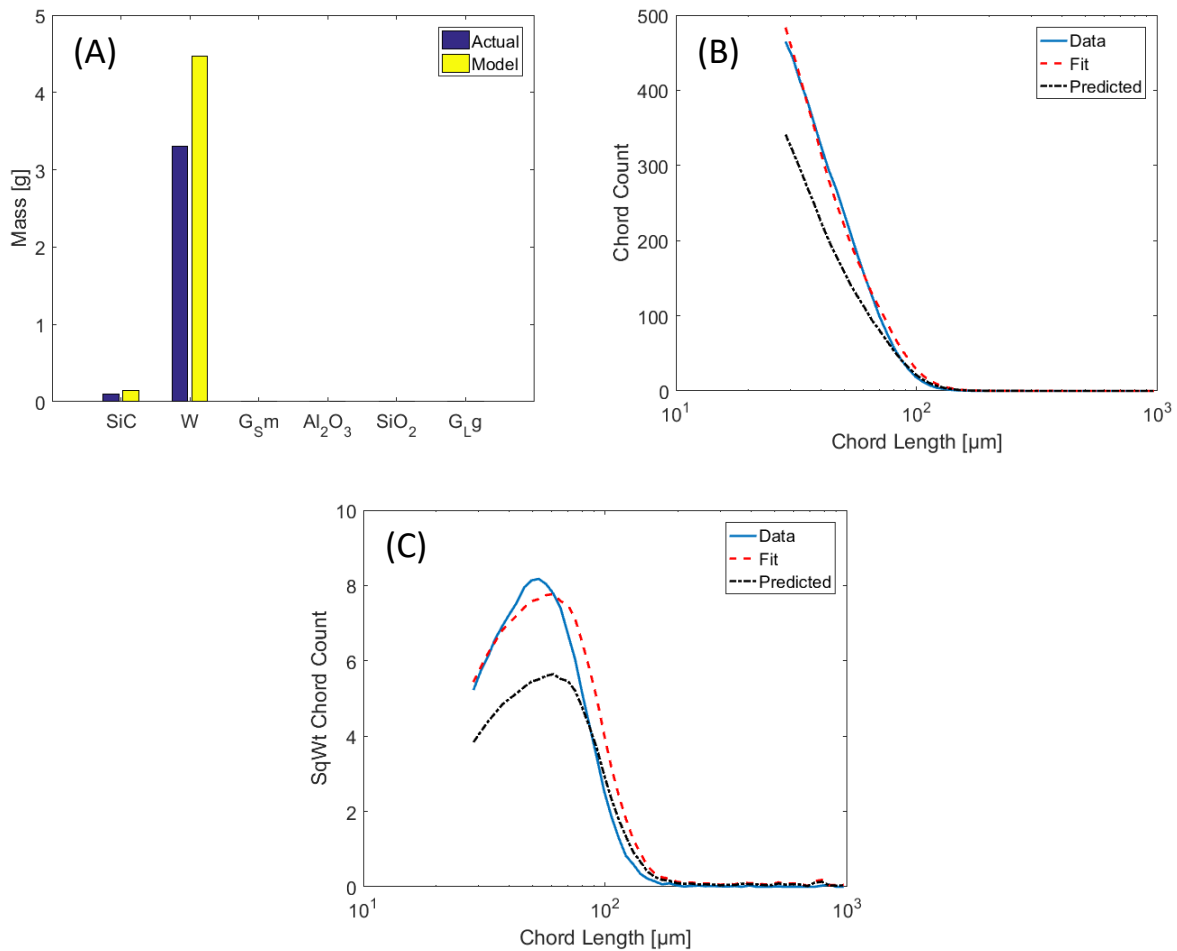


**Figure 26 – (A) Composition estimates for a mixture of 0.1 g SiC and 3.3 g tungsten, with square-weighted data in the model. Including the extra data set removes all of the excess amounts predicted in the unweighted-only model. This model incorporates the AIC and excludes counts smaller than 30 μm. (B) CLH plot of SiC-tungsten mixture. (C) CLH plot of SiC-tungsten mixture, using square-weighted data.**

Modifying the model to consider both types of weighting improved the model's estimate of the two-component system containing SiC and tungsten. This model's composition estimate is plotted in Figure 26A, alongside plots containing the system's CLH, the model's optimized fit of this CLH, and the model's prediction of the data using the system's known composition – CLH plots are provided for both unweighted (Figure 26B) and square-weighted (Figure 26C) histograms.

Adding square-weighted data to the model immediately improved the results for the SiC-tungsten system. The amounts of both components were overestimated, but all of the other components that were previously predicted to be present have been removed from the composition estimate. The reason for this improvement is found in Figure 26C, which shows that the model's predicted CLH (the black dotted-dashed curve) is similar in shape to the measured CLH (the solid blue curve). The total counts predicted by the model are lower than the data shows, but the similarity between the shape of the model predicted CLH and the data allows the model to compensate for the difference in counts by simply adding more of the components that are actually present to the estimate. The square-weighted data conforms more closely to the model's linear assumptions than the unweighted data for this system.

Despite the substantially improved estimation accuracy for the SiC-tungsten system, adding square-weighted data to the model negatively impacted the accuracy of the model in the glass-tungsten system. Figure 27A shows this model's composition estimate for the same mixture of two components used in Figure 19. The unweighted and square-weighted CLHs are plotted in Figures 27B and C respectively.

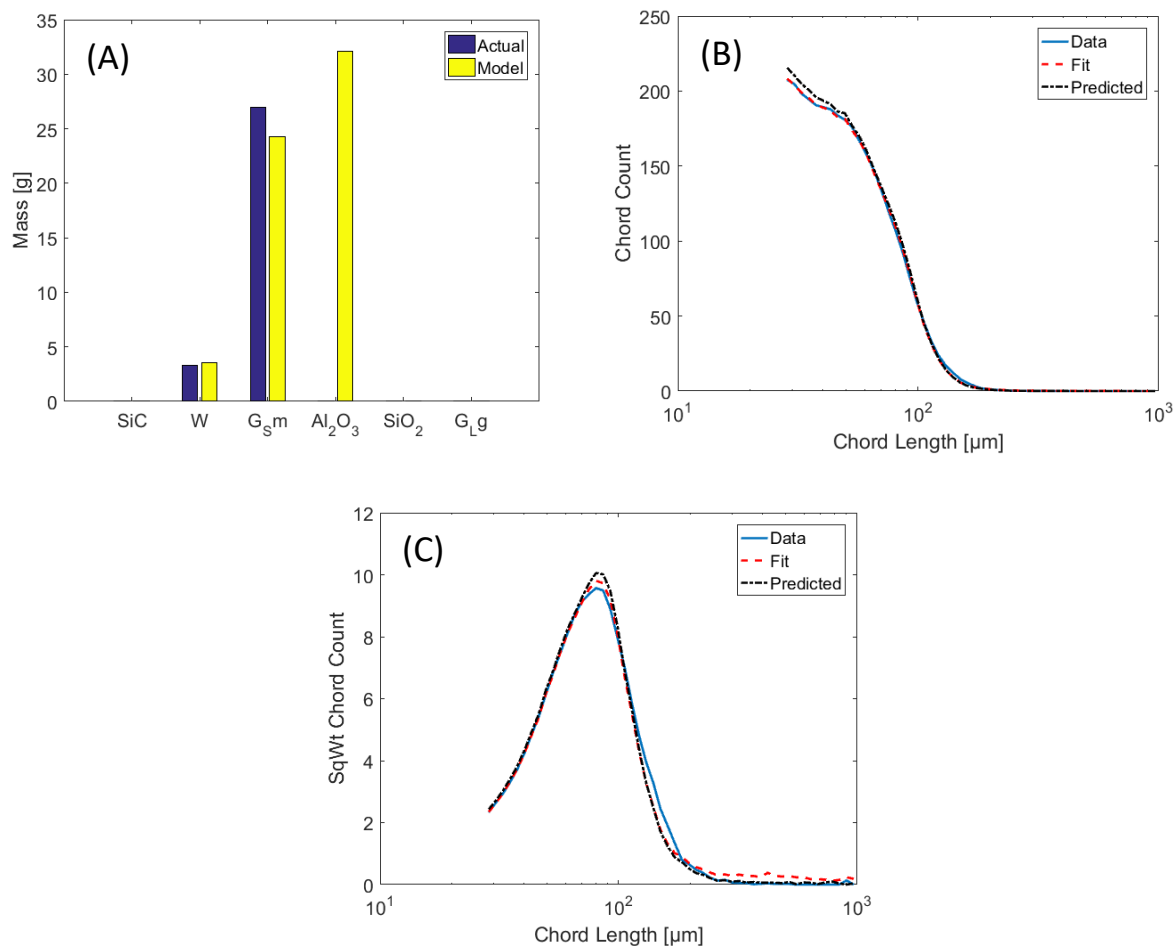


**Figure 27 – (A) Composition estimates for a mixture of 27 g small glass beads and 3.3 g tungsten, with square-weighted data in the model. (B) CLH plot of glass-tungsten mixture. (C) CLH plot using square-weighted data.**

Previously, the AIC had served as an effective means to balance goodness of fit with model simplicity. This allowed for alumina to be removed from the composition estimate. However, with both unweighted and square-weighted histograms in the model, the AIC no longer balances goodness of fit and simplicity, and the estimated mass of alumina returns. Adding the counts below 30 μm back into the model fit (not shown) did not improve the estimate. The masses of glass and tungsten were still estimated accurately, which indicates that their square-weighted histograms still conform to the linear model assumptions.

Lastly, Figure 28 shows the estimation results and CLH plots for the simulant, consisting of all six components. In this figure, the model is applied to the same data set used to create Figures 24 and 25.

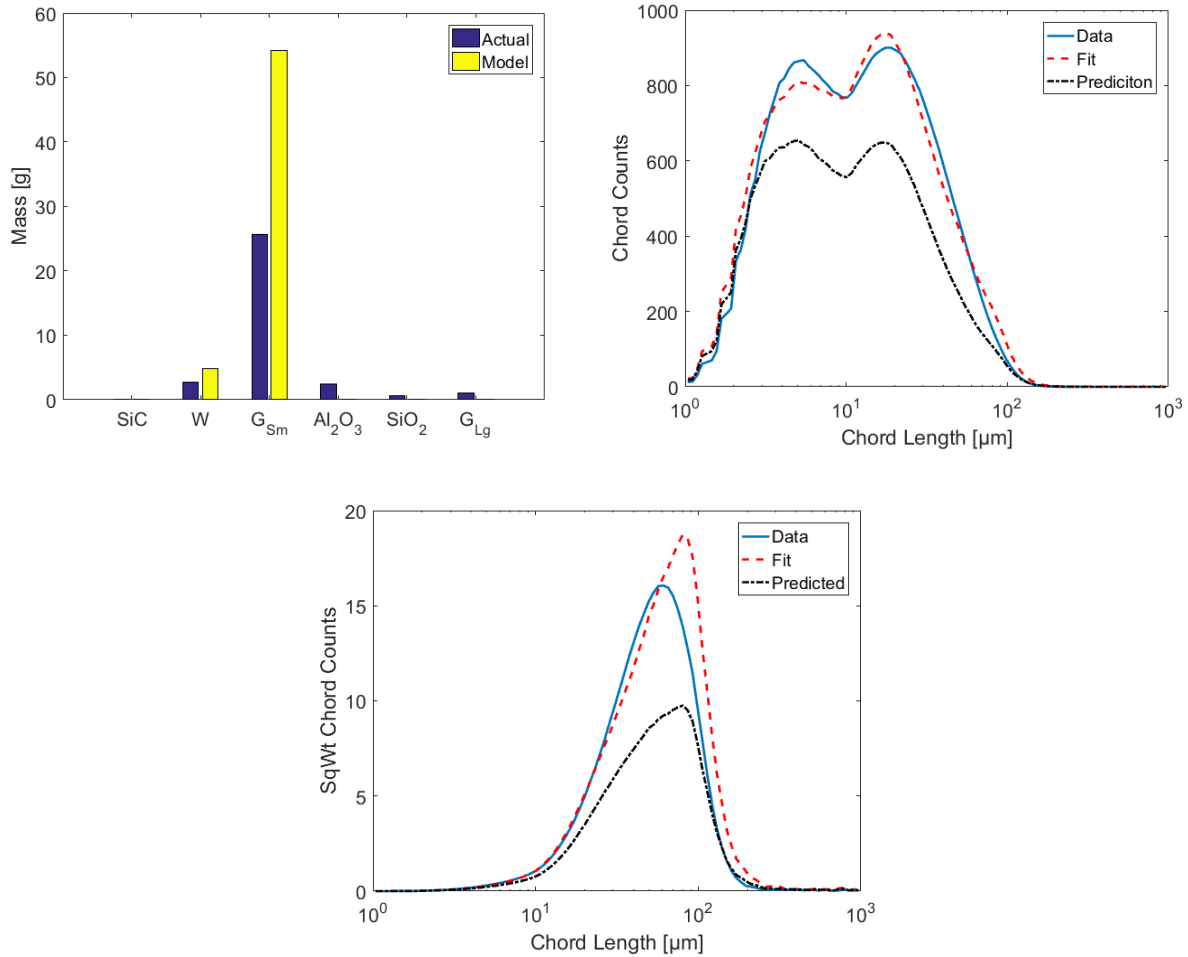


**Figure 28 – (A) Composition estimates for the completed simulant containing 0.1 g SiC, 2.7 g tungsten, 26 g small glass beads, 2.4 g alumina, 0.7 g silica, and 1 g large glass beads, with square-weighted data in the model. (B) CLH plot of this mixture. (C) CLH plot using square-weighted data.**

The composition plotted in Figure 28A is similar to the composition calculated without square-weighted data, shown in Figure 24. SiC (not visible on the plot due to the y-axis dimensions, but still present) was estimated accurately, while tungsten and the small glass beads were overestimated. All three large components were not seen – this is expected, as Figure 7 previously showed that the large components generate a shorter maximum chord length than the small

components. Square-weighting effectively amplifies the long chord counts, which for this simulant emphasizes the three smallest components. Unlike Figure 27, the data (solid blue curves) and the predictions (dotted dashed black curves) in Figure 28B and 28C do not match, indicating that a linear model is insufficient to describe the behavior of the entire simulant.

Adding square-weighted data to the model represents an accuracy trade-off – the model gains the ability to predict the composition of the SiC-tungsten system, but loses accuracy when examining the other small component pair. If silicon carbide is present in a mixture of this simulant, then square-weighting of the data is necessary; without this operation, the model would erroneously add other components to the fit to make up the difference between its CLH prediction and the observed data. However, as has been shown already in Figures 13 and 14, FBRM struggles to properly estimate the concentration of all but small amounts of silicon carbide in water. It would be preferable to use a different small component to represent such a small particles in the range of 1-10  $\mu\text{m}$  in nuclear waste, rather than including it in the simulant mixture and jeopardizing FBRM's ability to monitor the other five components. Particles of this size are present in the waste at the Hanford site, so selecting a new material to simulate these particles is necessary if FBRM is to be used in the experiments at NETL.

## CHAPTER 5. Conclusions and Recommendations

An empirical model for estimating the composition of complex, multi-species particulate slurries has been tested on a six-component mixture designed to approximate the radioactive waste at the Hanford site. The model adapts a framework previously used for particle size measurement<sup>[31]</sup> and instead uses it to calculate the abundance of each component in the simulant. The model uses constrained regression to find the linear combination of the components' characteristic FBRM histograms that best fits a given data set. Additional model characteristics were tested, such as selecting the optimal number of components based on the Akaike Information Criterion, to alleviate problems that arose with certain components.

Initial experiments with the six-component simulant showed difficulty in predicting the presence of each component from FBRM data, so the system was broken down into multiple smaller pairs. The model was most accurate when applied to a binary system of tungsten shavings and small glass beads in the range of 45-90  $\mu\text{m}$ . With this binary mixture, the model was able to estimate the masses of each component offline, using averaged FBRM data to remove noise, with accuracy up to  $\pm 18\%$  of the actual amounts. Applied to noisy data in real time, the model was able to track additions of the components into a mixture, with reduced accuracy compared to the case in which the CLH is averaged over time. Excluding fine counts (defined as chord counts shorter than 30  $\mu\text{m}$ ) improves the estimation accuracy to  $\pm 10\%$  for this binary system, but the amount of data discarded when removing these counts diminishes the model's capability when it is applied to mixtures containing any of three largest components.

The model tested in this thesis, which assumes a linear relationship between FBRM counts and particle mass, was unable to describe the behavior of silicon carbide particles outside of very

low slurry densities. Because of this known nonlinear behavior, the model was only tested on silicon carbide slurries at concentrations that behave linearly. Despite this measure, the model was still unable to form an accurate composition estimate of silicon carbide mixtures. The CLH from silicon carbide did not linearly add to the other component histograms, and silicon carbide mixtures consistently produced more FBRM counts than the linear model predicted. Adding square-weighted histograms to the model and forcing it to fit both unweighted and square-weighted data with its fingerprint histograms improved the estimation accuracy for silicon carbide; however, the component masses were still overestimated by 30% in a simple two-component mixture. This inaccuracy, combined with the square-weighted model's reduced performance when applied to mixtures of the other five components (adding square-weighted data makes the AIC less capable of selecting the components that are present in the mixture), suggests that square-weighted data should not be included in the model for analyzing mixtures of the simulant used in this work. To improve the accuracy, a nonlinear model is necessary to describe the behavior of silicon carbide.

Each of the three largest components (alumina, sand, and large glass beads) used in the waste simulant proved difficult to monitor with a linear FBRM model. All components produced observable chord counts when monitored in isolation, and the counts they produced increased linearly as more particles were added to the system. However, all three shared an overlapping CLH peak. The similarity of these components' CLHs around the peak impedes quantitative use of the FBRM data when they are mixed together. While the model was able to gauge the presence of two of the three large components in a mixture containing all of them, it was unable to estimate the amounts of each in said mixture.

When the model was applied to measured CLHs produced by the complete simulant, it was only able to predict the presence of the three smallest components. The amounts of these three

small components were overestimated – this is likely a consequence of silicon carbide’s nonlinear behavior, as its presence caused a nonlinear increase in chord counts in even a two-component mixture. The model was incapable of detecting the presence of any of the large components, but detecting their presence in mixtures with any of the small components is likely impossible with FBRM. All three large components produce at least an order of magnitude fewer counts per gram of material than the small components. Referring back to Table 2 in Section 4.1, none of the large components produced more chords than the standard chord count error in any of the small components. The low counts produced by the large components, which are potentially indistinguishable from noise when the small components are present, and the fact that all of the large components’ CLHs overlap completely with those of the small components, combine to severely impede the detectability of the large components in the simulant mixture. All three large components would need to be present in concentrations far exceeding those listed in Table 1 to be detected.

The linear empirical model’s ability to predict the composition of the two-component mixture of tungsten shavings and small glass beads is a significant result because it demonstrates an ability to quantitatively interpret FBRM data for mixtures of multiple particle types. Glass beads are translucent and poorly reflect light, which is shown in their micrographs in Figure 6. This makes them difficult to observe with FBRM; however, the empirical formulation used in this work is able to estimate their concentration in a mixture with opaque tungsten particles, which are more numerically dense. It should be noted that this work is significantly more challenging than previous quantitative studies where only mixtures containing a single solid species are considered, drawing a correlation between chord length and particle size for said species. The results shown for the two-component mixture of glass beads and tungsten shavings demonstrates that FBRM is

viable for quantitative use on multicomponent systems, and future work may find more systems that can be successfully measured by the linear framework presented in this thesis.

With regards to the waste simulant used in this work, it is recommended that nonlinear empirical modeling be used for future quantitative studies involving the simulant presented here. For the reasons discussed in Section 2.3.3, interpreting the FBRM data from the simulant using a first-principles approach is impractical. Nonlinear modeling would allow the concentration of silicon carbide, which exhibits chord count saturation behavior even at low concentrations, to be calculated at higher solid fractions than those used in this work. Including information about the interactions between silicon carbide and the other simulant components in the model would improve the composition estimates of multicomponent mixtures. Figures 22 and 26 show that a clear increase in total counts is observed when silicon carbide is combined with other solid species – this behavior is impossible to describe with a linear model. The chord count increase still allows for estimation that is accurate within the innate day-to-day variability of the FBRM systems (as discussed in Section 4.1), and the shape of the resultant histogram is consistent with the linear combination of the fingerprints. However because the chord counts increase by roughly the same amount each time silicon carbide is combined with the other components, it should be possible to improve the estimation accuracy for these mixtures with a nonlinear model.

Additionally, a change of simulant species is recommended if FBRM is to be used in future NETL experiments. The three largest components are not ideal reflectors, and if similarly sized particles are to be detected amidst the smallest components in the simulant, they must be composed of materials that reflect light more clearly. Mitigating chord splitting would allow the large components to generate chord counts much longer than those generated by the small components. Choosing new components in this way makes the large components detectable, even though they

are to be present in trace quantities and generate far fewer counts than the rest of the simulant. Because most of the particles in the Hanford waste are thought to be metallic,<sup>[3, 8]</sup> replacing the three large components with more opaque materials seems consistent with the real properties of the waste. The six components used in the current simulant are not all simultaneously detectable with FBRM, and the most straightforward way to alleviate this problem is by replacing the alumina, silica, and large glass beads with different materials.

## REFERENCES

1. *Hanford Quick Facts*. 2008 [cited 2017].
2. Fitzsimmons, T. and C. Findley, *Final Determination Pursuant to the Hanford Federal Facility Agreement and Consent Order (HFFACO) in the Matter of Disapproval of the Department of Energy's Change Control Form M-62-01-02*, W.D.o. Ecology and U. EPA, Editors. 2001.
3. Wells, B.E., et al., *Estimate of Hanford Waste Insoluble Solid Particle Size and Density Distribution*. 2007, Batelle - Pacific Northwest Division.
4. Kosson, D.S., et al., *Re: CRESP WTP PTF Technical Issues Review Team, Letter Report 1*, W. Hamel, Editor. 2013.
5. Restivo, M.L., et al., *Technology Evaluation for Conditioning of Hanford Tank Waste using Solids Segregation and Size Reduction*. 2014, Savannah River National Laboratory, Pacific Northwest National Laboratory.
6. Fountain, M.S., R.T. Brigantic, and R.A. Peterson, *Statistical Methods and Tools for Hanford Staged Feed Tank Sampling*. 2013, Pacific Northwest National Laboratory.
7. Wilkins, N. and R. Gimpel, *Waste Mineralogy and Particle Physical Property Characterization*. River Protection Project.
8. Wells, B.E., et al., *Hanford Waste Physical and Rheological Properties: Data and Gaps*. 2011, Pacific Northwest National Laboratory: Richland, WA.
9. Sheikhzadeh, M., M. Trifkovic, and S. Rohani, *Real-time optimal control of an anti-solvent isothermal semi-batch crystallization process*. *Chemical Engineering Science*, 2008. **63**(3): p. 829-839.

10. Abu Bakar, M.R., et al., *The impact of direct nucleation control on crystal size distribution in pharmaceutical crystallization processes*. Cryst. Growth Des., 2009. **9**(3): p. 1378.
11. Mitchell, N.A., P.J. Frawley, and C.T. O’Ciardha, *Nucleation kinetics of paracetamol-ethanol solutions from induction time experiments using Lasentec FBRM®*. J. Cryst. Growth, 2011. **321**: p. 91.
12. Mettler-Toledo. *ParticleTrack with FBRM Technology*. [cited 2016; Available from: [http://www.mt.com/us/en/home/products/L1\\_AutochemProducts/FBRM-PVM-Particle-System-Characterization/FBRM.html](http://www.mt.com/us/en/home/products/L1_AutochemProducts/FBRM-PVM-Particle-System-Characterization/FBRM.html)].
13. Larsen, P.A., J.B. Rawlings, and N.J. Ferrier, *An algorithm for analyzing noisy, in situ images of high-aspect-ratio crystals to monitor particle size distribution*. Chem. Eng. Sci., 2006. **61**: p. 5236.
14. Presles, B., et al., *Novel image analysis method for in situ monitoring the particle size distribution of batch crystallization processes*. J. Electron. Imaging, 2010. **19**: p. 031207.
15. Wang, X.Z., K.J. Roberts, and C. Ma, *Crystal growth measurement using 2D and 3D imaging and the perspectives for shape control*. Chem. Eng. Sci., 2008. **63**(5): p. 1173.
16. Yu, Z.Q., et al., *Recent Advances in Crystallization control*. Chemical Engineering Research and Design, 2007. **85**(7): p. 893-905.
17. Meyer, P.A., et al., *Pulse Jet Mixing Tests With Noncohesive Solids*. 2009, Pacific Northwest National Laboratory.
18. Fort, J.A., et al., *Scaled Testing to Evaluate Pulse Jet Mixer Performance in Waste Treatment Plant Mixing Vessels*, in *WM2010 Conference*. 2010, Pacific Northwest National Laboratory: Phoenix, AZ.

19. U.S. Department of Energy Approach for Resolution of Pulse-Jet-Mixed Vessel Technical Issues in the Waste Treatment and Immobilization Plant. 2014, US DOE Office of River Protection: Richland, WA. p. 42.
20. Townson, P.S. and M.G. Thien, *Design and Fabrication of Test Facilities for the Demonstration of Jet Mixer Performance in the Hanford Double Shell Tanks - 11241*, in *WM2011 Conference*. 2011: Phoenix, AZ.
21. Thien, M.G., D.A. Greer, and P.S. Townson, *Estimating High Level Waste Mixing Performance in Hanford Double Shell Tanks - 11193*, in *WM2011 Conference*. 2011: Phoenix, AZ.
22. Tadayyon, A. and S. Rohani, *Determination of Particle Size Distribution by Par-Tec® 100 Modeling and Experimental Results*. Part. Part. Syst. Charact., 1998(15): p. 127-135.
23. Tadayyon, A. and S. Rohani, *Control of fines suspension density in the fines loop of a continuous KCl crystallizer using transmittance measurement and an FBRM® probe*. The Canadian Journal of Chemical Engineering, 2000. **78**(4): p. 663-673.
24. Fujiwara, M., et al., *Paracetamol Crystallization Using Laser Backscattering and ATR-FTIR Spectroscopy: Metastability, Agglomeration, and Control*. Cryst. Growth Des., 2002. **2**(5): p. 363-370.
25. Heath, A.R., et al., *Estimating Average Particle Size by Focused Beam Reflectance Measurement (FBRM)*. Part. Part. Syst. Charact., 2002(19): p. 84-95.
26. O'Sullivan, B. and B. Glennon, *Application of in Situ FBRM and ATR-FTIR to the Monitoring of the Polymorphic Transformation of D-Mannitol*. Org. Process Res. Dev., 2005(9): p. 884-889.

27. Schöll, J., et al., *In Situ Monitoring and Modeling of the Solvent-Mediated Polymorphic Transformation of l-Glutamic Acid*. *Crystal Growth & Design*, 2006. **6**(4): p. 881-891.
28. Barthe, S.C., M.A. Grover, and R.W. Rousseau, *Observation of Polymorphic Change through Analysis of FBRM Data: Transformation of Paracetamol from Form II to Form I*. *Crystal Growth & Design*, 2008. **8**(9): p. 3316-3322.
29. Kail, N., H. Briesen, and W. Marquardt, *Analysis of FBRM measurements by means of a 3D optical model*. *Powder Technol.*, 2008. **185**(3): p. 211.
30. Kail, N., H. Briesen, and W. Marquardt, *Estimation of Particle Size Distributions From Focused Beam Reflectance Measurements Based on an Optical Model*. *Chem. Eng. Sci.*, 2009. **64**: p. 984-1000.
31. Li, H., et al., *Development of an empirical method relating crystal size distributions and FBRM measurements*. *Chem. Eng. Sci.*, 2013. **89**: p. 142.
32. Townson, P.S., et al., *Instrumentation for Real Time Monitoring of the 3-Dimensional Particulate Distribution in the Hanford Double Shell Tank Small Scale Mixing Demonstration Platform - 11242*, in *WM2011 Conference*. 2011: Phoenix, AZ.
33. Ruf, A., J. Worlitschek, and M. Mazzotti, *Modeling and Experimental Analysis of PSD Measurements through FBRM*. *Part. Part. Syst. Charact.*, 2000(17): p. 167-179.
34. Yu, Z.Q., P.S. Chow, and R.B.H. Tan, *Interpretation of Focused Beam Reflectance Measurement (FBRM) Data via Simulated Crystallization*. *Organic Process Research & Development*, 2008. **12**(4): p. 646-654.
35. Doki, N., et al., *Process Control of Seeded Batch Cooling Crystallization of the Metastable  $\alpha$ -Form Glycine Using an In-Situ ATR-FTIR Spectrometer and an In-Situ FBRM Particle Counter*. *Crystal Growth & Design*, 2004. **4**(5): p. 949-953.

36. Zhao, J., et al., *Monitoring the Polymorphic Transformation of Imidacloprid Using in Situ FBRM and PVM*. Organic Process Research & Development, 2013. **17**(3): p. 375-381.
37. Su, W., et al., *The Impact of Operating Parameters on the Polymorphic Transformation of d-Mannitol Characterized in Situ with Raman Spectroscopy, FBRM, and PVM*. Organic Process Research & Development, 2010. **14**(6): p. 1432-1437.
38. Nagy, Z.K., et al., *Determination of the kinetic parameters for the crystallization of paracetamol from water using metastable zone width experiments*. Ind. Eng. Chem. Res., 2008. **47**: p. 1245.
39. Mitchell, N.A., C.T. Ó'Ciardhá, and P.J. Frawley, *Estimation of the growth kinetics for the cooling crystallisation of paracetamol and ethanol solutions*. Journal of Crystal Growth, 2011. **328**(1): p. 39-49.
40. Aamir, E., et al., *Combined Quadrature Method of Moments and Method of Characteristics Approach for Efficient Solution of Population Balance Models for Dynamic Modeling and Crystal Size Distribution Control of Crystallization Processes*. Ind. Eng. Chem. Res., 2009. **48**: p. 8575.
41. Ochsenein, D.R., et al., *Growth Rate Estimation of  $\beta$  l-Glutamic Acid from Online Measurements of Multidimensional Particle Size Distributions and Concentration*. Ind. Eng. Chem. Res., 2014. **53**: p. 9136.
42. Saleemi, A., C. Rielly, and Z.K. Nagy, *Automated direct nucleation control for in situ dynamic fines removal in batch cooling crystallization*. CrystEngComm, 2012. **14**(6): p. 2196.

43. Saleemi, A.N., C.D. Rielly, and Z.K. Nagy, *Comparative investigation of supersaturation and automated direct nucleation control of crystal size distributions using ATR-UV/vis spectroscopy and FBRM*. Cryst. Growth Des., 2012. **12**(4): p. 1792.
44. Woo, X.Y., et al., *Adaptive Concentration Control of Cooling and Antisolvent Crystallization with Laser Backscattering Measurement*. Crystal Growth & Design, 2009. **9**(1): p. 182-191.
45. Chew, J.W., P.S. Chow, and R.B.H. Tan, *Automated In-line Technique Using FBRM to Achieve Consistent Product Quality in Cooling Crystallization*. Cryst. Growth Des., 2007. **7**: p. 1416.
46. Hermanto, M.W., P.S. Chow, and R.B.H. Tan, *Operating Strategy to Produce Consistent CSD in Combined Antisolvent-Cooling Crystallization using FBRM*. I&EC Research, 2012. **51**: p. 13773-13783.
47. Griffin, D.J., et al., *Feedback Control of Multicomponent Salt Crystallization*. Cryst. Growth Des., 2015. **15**: p. 305-317.
48. O'Sullivan, B., et al., *In Situ Monitoring of Polymorphic Transitions*. Org. Process Res. Dev., 2003(7): p. 977-982.
49. Simmons, M.J.H., P.A. Langston, and A.S. Burbidge, *Particle and Droplet Size Analysis from Chord Distributions*. Powder Technol., 1999. **102**(1): p. 75-83.
50. Griffin, D.J., et al., *Data-Driven Modeling and Dynamic Programming Applied to Batch Cooling Crystallization*. I&EC Research, 2016. **55**: p. 1361-1372.
51. Yu, W. and K. Erickson, *Chord Length Characterization Using Focused Beam Reflectance Measurement Probe - Methodologies and Pitfalls*. Powder Technol., 2008. **185**: p. 24-30.

52. Heinrich, J. and J. Ulrich, *Application of Laser-Backscattering Instruments for In Situ Monitoring of Crystallization Processes - A Review*. Chemical Engineering & Technology, 2012. **35**(6): p. 967-979.
53. David Greaves, J.B., James Mulligan, Alberto Montesi, Jefferson Creek, E. Dendy Sloan, Carolyn A. Koh, *Measuring the particle size of a known distribution using the focused beam reflectance measurement technique*. Chemical Engineering Science, 2008(63): p. 5410-5419.
54. Li, M., D. Wilkinson, and K. Patchigolla, *Comparison of Particle Size Distributions Measured Using Different Techniques*. Part. Sci. and Tech., 2005. **23**(3): p. 265-284.
55. Li, M. and D. Wilkinson, *Determination of Non-spherical Particle Size Distribution from Chord Length Measurements. Part 1: Theoretical Analysis*. Chem. Eng. Sci., 2005(60): p. 3251-3265.
56. Li, M. and D. Wilkinson, *Determination of Non-spherical Particle Size Distribution From Chord Length Measurements. Part 2: Experimental Validation*. Chem. Eng. Sci., 2005(60): p. 4992-5003.
57. Mangold, M., *Use of a Kalman Filter to Reconstruct Particle Size Distributions from FBRM Measurements*. Chem. Eng. Sci., 2012. **70**: p. 99-108.
58. Hukkanen, E.J. and R.D. Braatz, *Measurement of Particle Size Distribution in Suspension Polymerization Using in situ Laser Backscattering*. Sens. Actuators, B, 2003. **96**: p. 451.
59. Vay, K., W. Friess, and S. Scheler, *Understanding Reflection Behavior as a Key for Interpreting Complex Signals in FBRM Monitoring of Microparticle Preparation Processes*. Int. J of Pharm., 2012(437): p. 1-10.

60. Senaputra, A., et al., *Focused beam reflectance measurement for monitoring the extent and efficiency of flocculation in mineral systems*. *AICHE Journal*, 2014. **60**(1): p. 251-265.
61. Czapla, F., et al., *Application of a recent FBRM-probe model to quantify preferential crystallization of DL-threonine*. *Chem. Eng. Res. Des.*, 2010. **88**: p. 1494.
62. Togkalidou, T., et al., *Parameter Estimation and Optimization of a Loosely Bound Aggregating Pharmaceutical Crystallization Using in Situ Infrared and Laser Backscattering Measurements*. *Ind. Eng. Chem. Res.*, 2004. **43**(19): p. 6168.
63. Wynn, E.J.W., *Relationship Between Particle-Size and Chord-Length Distributions in Focused Beam Reflectance Measurement: Stability of Direct Inversion and Weighting*. *Powder Technol.*, 2003. **133**(1-3): p. 125-133.
64. Li, H., et al., *Modeling of Nucleation and Growth Kinetics for Unseeded Batch Cooling Crystallization*. *Industrial & Engineering Chemistry Research*, 2017. **56**(14): p. 4060-4073.
65. Li, H., et al., *Application of an empirical FBRM model to estimate crystal size distributions in batch crystallization*. *Cryst. Growth Des.*, 2014. **14**: p. 607.
66. Grover, M.A., S.C. Barthe, and R.W. Rousseau, *Principal Component Analysis for Estimating Population Density from Chord-Length Density*. *AICHE J.*, 2009. **55**(9): p. 2260-2270.
67. Worlitschek, J., T. Hocker, and M. Mazzotti, *Restoration of PSD from chord length distribution data using the method of projections onto convex sets*. *Part. Part. Syst. Charact.*, 2005. **22**: p. 81.
68. Barthe, S. and R.W. Rousseau, *Utilization of Focused Beam Reflectance Measurement in the Control of Crystal Size Distribution in a Batch Cooled Crystallizer*. *Chemical Engineering & Technology*, 2006. **29**(2): p. 206-211.

69. Nere, N.K., et al., *Transformation of the Chord-Length Distributions to Size Distributions for Nonspherical Particles with Orientation Bias*. *Ind. Eng. Chem. Res.*, 2007. **46**: p. 3041.
70. Bamberger, J.A., et al., *Hanford Tank Farms Waste Certification Flow Loop Test Plan for Instrument Evaluation*. 2010, Pacific Northwest National Laboratory.
71. Guenther, C., *NETL simulant composition*, R.W. Rousseau, Editor. 2015.